POLITECNICO DI TORINO

Master's Degree in Electronic Engineering

Master's Degree Thesis

Development of an autonomous plant monitoring system based on Plant Microbial Fuel Cells

Supervisors

Prof. Danilo DEMARCHI

PhD. Umberto GARLANDO

Candidate

FRANCESCA ANGELINI

DECEMBER 2021

Summary

The objective of this thesis is to propose an autonomous receiving system, which is part of a sensor node for plant health monitoring. The latter is meant to be used in the Internet of Things (IoT) for collecting data in agricultural applications so that the farmers can be provided with real-time information from the fields. In this way, they can take advantage of actual knowledge of the plants' status to make the best decision for the optimization of the resources having as objective the enhancement of the sustainability and the efficiency in the management of the crops. The reasons behind the rapid diffusion of these wireless sensor networks are widely reviewed in the first chapter of this dissertation.
The second chapter deals with the environmental sources of energy that can be used to replenish the sensor nodes to ensure a long-term autonomous operation. The focus is placed on Plant Microbial Fuel Cells, a green technology that exploits the microbial activity at the plant's roots (rhizosphere region) to produce bioelectricity. Thanks to the addition to the basic technology (i.e., microbial fuel cell) of the plants, which continuously provide organic substrate to be converted into electricity, the amount of power extracted from PMFC only recently has been demonstrated to be sufficient to sustain the operation of ultra-low-power sensor nodes.
The description of the implemented PMFC based on tobacco plants is presented in Chapter 3, together with the characterization of the cell, which gives an idea of the extractable amounts of power and current.
Chapter 4 is dedicated to the description of the receiving system's components, from the ultra-low-power custom board which embeds the controller and LoRa transceiver units to the power management system (PMS) that has been employed to extract the energy from the PMFC and manage the storage of the energy in a supercapacitor.
A power management strategy has been adopted to increase the lifetime of the node. It is presented in Chapter 5 and consists in exploiting the low-power modes of the microcontroller. Indeed, the receiving system measures the frequency of an oscillating signal sent to the microcontroller by a transmitting system implemented in one previous work of the MiNES group. According to the study on which that work is based, the frequency at which the signal propagates along the plant stem

(proportional to its electrical impedance) should give information about the plant's watering status, allowing optimized water use. Since the plant status changes slowly during the day, frequent measurements are not needed. Thus the microcontroller is normally in stop mode, and it is awakened by the interrupt of the GPIO pin when a signal is received and thus a measurement must be performed, or by a timing system when a packet of data must be sent wirelessly through the LoRa transceiver. To this purpose, the microcontroller executes a C code developed from the firmware provided with the Murata module, which will be described in Chapter 5 as well.
Chapter 6 is dedicated to the system's power performances description obtained through real measurements in each operating state, together with considerations about the possibility of powering it with the energy level extracted from the PMFC. The current requirements of the receiving system are shown in figure 1, where a measurement is performed every ten minutes, while a packet is sent every 45 minutes to the gateway. The consumption is reduced to only 1.45 μA (not visible in the figure because too small with respect to the consumption peaks) when the MCU is in stop mode. Figure 2 shows the voltage on the storage element attached to the PMS during a 19 hours interval of system operation. It can be observed that when the voltage monitoring starts, the storage element is charging. Once the maximum set voltage (4.2 V) is reached, the voltage remains around this value, demonstrating that the energy harvesting system can sustain the autonomous operation of the sensor node. The improvements that could be applied to the system to make it more durable and efficient will be presented in Chapter 6 as well.

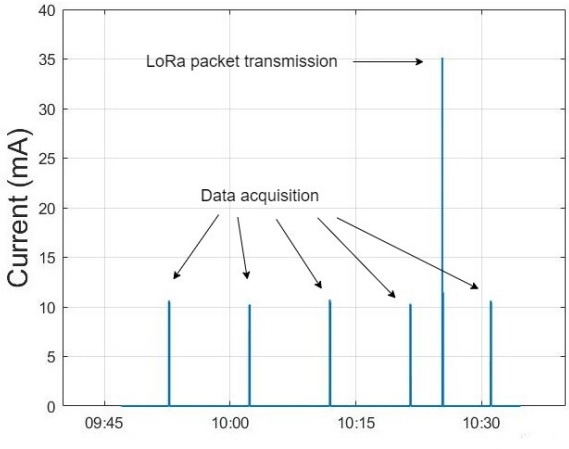

Figure 1: Current consumption in the different microcontroller operating states.

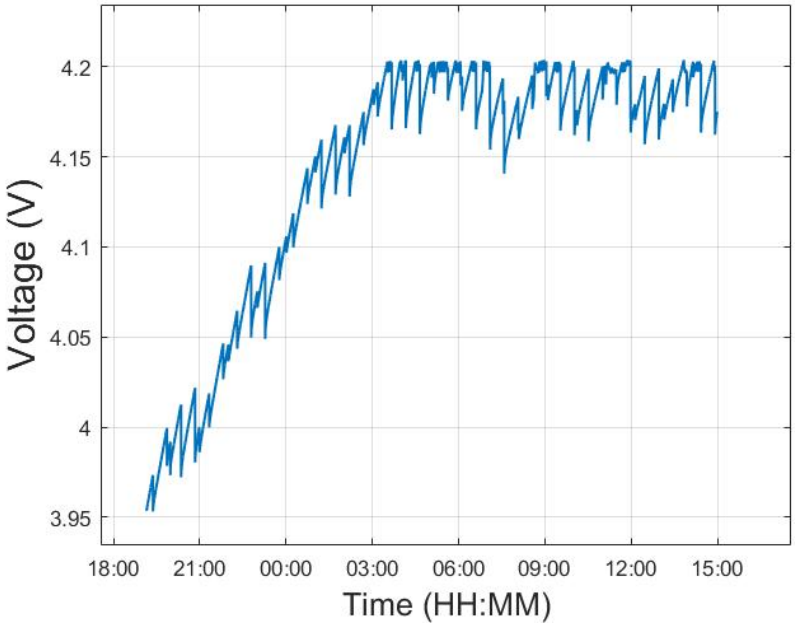

Figure 2: Voltage on the storage element during system operation.

Acknowledgements

"Ai miei genitori"

Table of Contents

List of Tables

List of Figures

Acronyms

IoT
Internet of Things

WSN
Wireless Sensor Network

MFC
Microbial Fuel Cell

PMFC
Plant Microbial Fuel Cell

MPPT
Maximum Power Point Tracking

PEM
Proton Exchange Membrane

PMS
Power Management System

LoRa
Long-Range protocol

LoRaWAN
Long-Range Wide Area Network

GPIO
General Purpose I/O

OTAA

Over-The-Air Activation

TTN

The Things Network

Chapter 1

Motivation

Among the central themes of the new millennium, there is undoubtedly food security. Indeed, nowadays, food production and agriculture are seriously threatened by the world's population growth. Even though the growth rate of the world's population has slowed since the end of the last century and is expected to slow further through the end of this century, actual projections state that by 2050 the global population will reach 9.7 billion people and 10.9 billion by 2100 [1].
Besides feeding these additional 2 billion people with respect to the 7.7 billion living on the planet today, agriculture must face another challenge: global climate change, with more common extreme events, higher temperatures, and reduced precipitations. Based on agriculture, food production is a victim of these rapid and alarming transformations and one of the main drivers. As explained in [2], the primary process contributing to this change is deforestation, since it causes the conversion of the chemical energy stored in the plants into heat and, therefore, can be seen as the opposite process with respect to photosynthesis. When the cleared green matter oxides, the heat released by the conversion of carbon into carbon dioxide is gained by climate, and the Earth's surface raises its temperature.
The authors in [2] also show that the population size is a variable dependent on the biosphere's farmland size since as farmlands increase, the carrying capacity increases. The increasing population size leads, in turn, to increasing energy demand. Deforestation can thus be seen as the regulator of world population growth and energy production. The combustion of fossil fuels, which represent the world's primary energy source, produces heat and carbon dioxide, gained, again, by the environment. These two interconnected mechanisms make deforestation the cause of 36% of total heat added to the surface until 1990. In figure 1.1, extracted from [2], the projections on the population size evolution depending on the trend of deforestation are shown. It can be observed how, if deforestation continues to decrease linearly at the current rate, the estimated values are very similar to the previously mentioned ([1]), while if it remains constant at the present value, the

world's population may reach 14.5 billion in 2100.

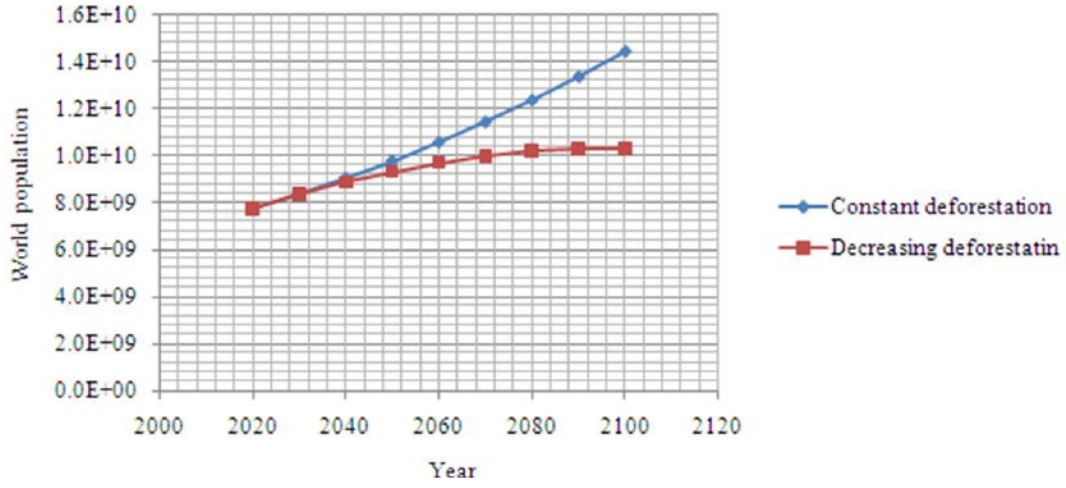

Figure 1.1: Expected world's population growth considering decreasing deforestation rate and constant deforestation rate (0.08% annually)

Undoubtedly the impact of humankind on the planet is enormous, with, today, approximately one-half of the Earth's vegetated lands used to grow food [3]. Finite natural resources are shrinking due to expanding deforestation and clearing of lands to transform them into farmlands, as a consequence of the increasing food demand and urbanization. Never as in the Anthropocene, the new geological epoch that humanity has entered, the pressure of humans on the planet has been so high, with agriculture being the single largest contributor to the global environmental change [4].
The increased emission of greenhouse gases, together with water pollution and biodiversity loss caused by nonsustainable agriculture methods, have brought to the erosion and the infertility of previously arable soils, threatening global food supplies. This degradation of lands can be associated in particular with the shift in agricultural methods, since about the 1960s, towards more industrialized practices. These new methods have been introduced with the primary (if not the only) objective of raising productivity without caring about sustainability. In [5] is explained how the intensification of production cycles and the indiscriminate use of synthetic fertilizers and pesticides has brought to the contamination of soils and groundwater resources due to the leaching of agrochemicals and nutrients.
The decline of water resources, vital for farming, also limits the world's crop production capacity. 70% of the global freshwater withdrawals is used for agriculture [6], being the first consumer in the world.

In this dramatic scenario, a revolution of agriculture towards sustainability is essential. As stated in [4], the two goals that must be pursued in this food revolution are to intensify sustainable agricultural practices to fulfill human needs and to do it without overcoming boundaries of biophysical processes that could lead to an unstable Earth system operating not safely. In this sense, traditional methods can be complemented with rapidly evolving intelligent products that can help us to manage natural resources in an optimal way, minimizing the inputs and obtaining the highest yield.

1.1 Thesis organization

In the next section, an introduction about the so-called Smart Farming will be given together with a brief review of the present technologies' state-of-the-art. This agricultural revolution introduces the issue of batteries to power the sensor nodes. The energy harvesting from environmental sources, which represents the most promising technique to solve this problem, will be presented in Chapter 2, focusing on Plant Microbial Fuel Cell. In Chapters 3 and 4, the energy harvester and the system implementations will be described. Chapter 5 will deal with the application code developed to manage power in an optimized way. Tests on the PMFC's energy performances and the possibility of sustaining the operation of the node with the output energy will be presented in Chapter 6. The possible improvements that could be applied to the system will also be described in this chapter.

1.2 WSNs for smart farming

To use in a sustainable way the shrinking natural resources agriculture must nowadays move towards the so-called Precision or Smart Farming, that allows the precise management of agricultural inputs thanks to the use of wireless technology. Wireless sensor networks (WSNs) have indeed gained more and more popularity in recent years, pushed mainly by the development of the Internet of Things (IoT) technology, which can be seen as a massive, distributed measurement system that is based on the exchange of data between world-wide interconnected objects [7]. WSNs can be seen as collaborative systems constituted of a series of low-cost, smart sensor nodes that communicate with one another through wireless interfaces. Their main purpose is to sense and gather data from the surroundings in environmental applications. As many other applications field, such as the biomedical field where these networks can be used to monitor patient health status, or the public safety and military field where they can be used for structural monitoring, farming can take advantage of WSNs to accurate monitor crop health status and development

stages, as well as climate conditions.
Analyzing and processing the collected data is possible to provide farmers with real-time information from the fields that can help anticipate dangers, like exceptional climate events, and optimize resources. In general, farmers can be supported by this information in making decisions in terms of irrigation, tillage, pesticides, and fertilizers spraying and seeding [8]. Further, the application of technology to agriculture aims to increase precision and efficiency in the processes of seeding and harvesting, as well as in crop sensing, through the automation of farms' machinery [9]. Smart agriculture (or Precision agriculture), taking advantage of smart sensors and communication engineering blended with cloud storage, aims to minimize the use of resources while increasing efficiency and quality but also trying to minimize the impact on the environment.

1.2.1 State-of-the-art

In this section, a brief overview of the recent works related to the monitoring of agricultural parameters through the use of sensor networks is given. Measuring water content in the soil for scheduling irrigation is of prime importance in farming. In most of the arid and semi-arid regions, such as Egypt, agriculture is the major income for most of the population. For this reason, the work presented in [10] aims to monitor with a low-cost solution the soil moisture in order to provide farmers with a solid base to optimize water use instead of basing decisions on their personal experience.
The system presented in this paper consists of a group of sensors to measure soil moisture, air humidity, and temperature together with a microcontroller and an SD card to collect the data. The sensors were calibrated in specifically prepared soil samples. Then the experiments were carried out in a greenhouse cultivated with cucumber. On the roof of it, photovoltaic panels were mounted to power the smart system. The soil moisture sensor is capacitive and consists of two parallel copper layers on a printed circuit board. Thanks to the soil mulching, the typical effect of soil temperature on the measured water content with capacitance-based sensors was reduced. This system constitutes an effective and low-cost solution to detect irrigation events and together measure environmental parameters and, thanks to the storage of data, can be used in intelligent irrigation systems to optimize the use of water resources.

With the same aim of continuously monitoring the soil moisture content, the authors in [11] propose an IoT system based on LoRaWAN wireless network that uses a soil probe with a printed capacitive sensor element to measure soil moisture. A sensor module, connected externally to the housing where the electronic unit

is sealed, also monitors the temperature and humidity of the microclimate. The acquired data are transmitted to the local gateway and stored in a database.
Four types of sensors consisting of interdigitated electrodes, as shown in figure 1.2, extracted directly from [11], were fabricated using different materials (copper, silver paste, and carbon-based materials) by etching or printing on a glass-epoxy substrate. Three out of four materials showed good sensitivity in measuring soil moisture in real soil samples, but the really interesting result was given by the design with a carbon-based material sensor element printed on a wooden plank. This environmentally friendly type of probe (metal-free printed element on a recyclable substrate) was successfully used and demonstrated the possibility to replace traditional materials with new eco-friendly, biodegradable materials.

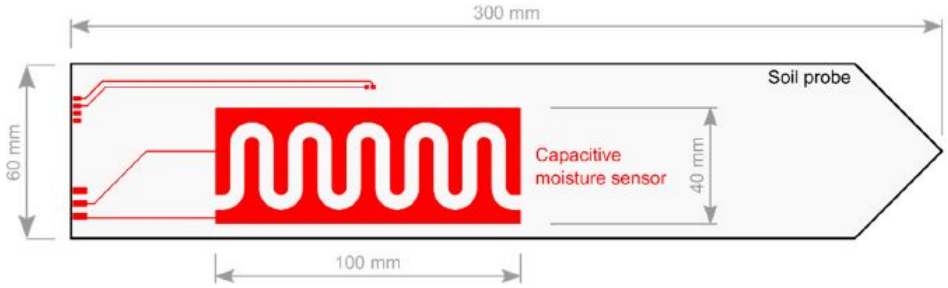

Figure 1.2: Capacitive sensor element printed on the soil probe.

Authors in [12] present a system that combines the measurement of the soil moisture with a web-based application to analyze the real-time data and a mobile application that allows farmers to have a continuous connection with the system. This low-cost system was installed in three villages of Thailand with different crop cultivation to demonstrate that this technology can be employed in any type of agriculture. The sensors, connected to a control box, collect data on humidity and soil moisture content, while the temperature is derived from a web service. A solenoid valve allows the water flow to be switched on/off.
A web-based application using Wi-Fi connection to access the internet was developed to process the information from the IoT devices and to allow an administrator to manage crop watering. The large amount of collected data is analyzed through data mining to find association rules among climate, soil properties, and crop yield. Thanks to this knowledge, the watering can be optimized for each specific cultivation in any season. Further, thanks to the designed mobile application, also the farmer can switch on/off the water flow manually or using an automatic method based on the collected data.

The use of agrochemicals in agriculture poses a worrying threat to human health and the environment, but still today, the spraying of herbicides over the fields remains the most common method of weed control, also raising the issue of increasing weed resistance to these types of products. Addressing this problem, the authors in [13] present a plant discrimination system based on spectral reflectance. Using two laser combinations modules and an optical cavity, the plant leaf is sequentially illuminated with laser beams of different wavelengths (with an intensity lower than the threshold intensity that could damage the leaf). Plants can be identified by processing the reflected signals from the leaf from each wavelength that are recorded by a scan image sensor. The authors tested the system mounted on a quad bike traveling a 7.5km/h in an outdoor canola field, using an aluminum shade and a plastic shroud to reduce the effect of daylight. The crops were discriminated from the wild radish with an accuracy of 90%. This optoelectronic-based sensor can be used together with a DGPS (Differential Global Positioning System) to log the coordinates of the detected target plant or to open the valve of a spray unit, as shown in figure 1.3, taken directly from [13], in order to avoid using herbicides on crops.

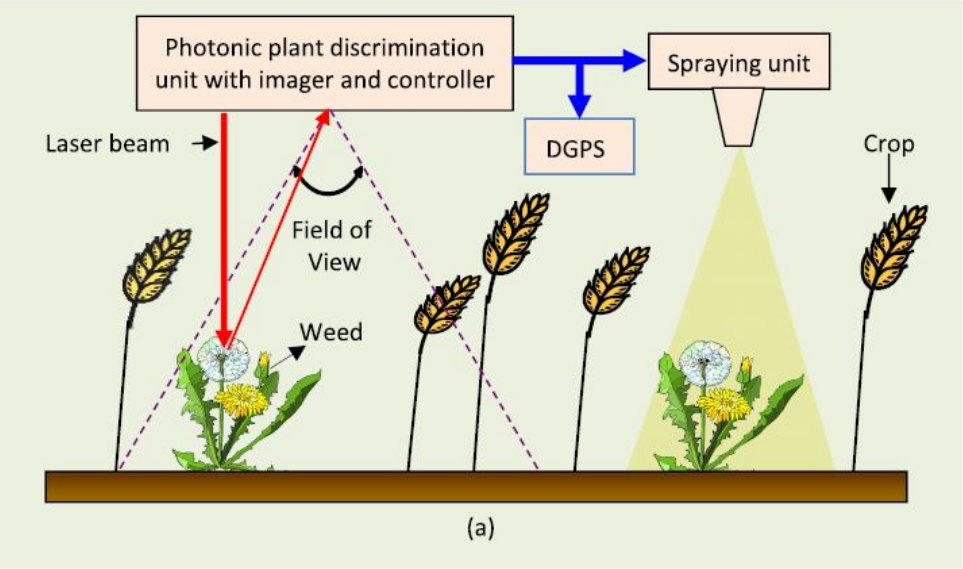

Figure 1.3: Spectral-reflectance-based sensor used for plant identification. A signal is generated by a control circuit to record the coordinates through a DGPS system or to activate a spray unit.

Authors in [9] propose another system that can be utilized for crop localization.

In addition to allowing automatic and precise removal of weeds, the authors' objective is to precisely measure plant spacing to treat each plant individually. An experimental platform was set up in a laboratory on which two non-invasive sensors were mounted: IR light-beam sensors, whose data are collected by a microcontroller, and a LiDAR laser scanner, using a computer through Ethernet cable to record data. 3D printed plants mounted on a conveyor chain moving at a constant speed were used in the laboratory test. An additional kinetic sensor that captures RGB images was employed in the field test, carried out on a tomato field using another specifically designed platform attached to a tractor.
The plant position was determined with a precision of 98% in the field test. As stated by the authors, the light-beam sensor represents a better choice when this technology must be used in real-time applications since the data furnished by the LiDAR sensor are characterized by high volume and complexity, not to mention the higher cost of the sensor.

The application of WSNs in smart agriculture can help to solve the problem of monitoring agro-meteorological parameters in remote areas or zones not served by communication networks (as large portions of the Appennini mountains in Italy). The demonstration of such a use can be found in the system presented in [8]: a sensor called AgriLogger, which measures temperature and humidity of the air, used together with a UAS (Unmanned Aerial Systems) vehicle that, in this case, is a customized drone that can fly autonomously thanks to a software control. The drone, using a GNSS (Global Navigation Satellite System) system, identifies the preselected area and, through a gripper transport system, can place the sensor remotely, replace the battery, and remove the sensor.
The RF transmitter mounted on the drone, thanks to the stimulation of the resonant system of the sensor through a directive antenna, can wake up the device. The host computer, thanks to a BLE (Bluetooth Low Energy) transceiver, can request the upload of the collected data, acting as a gateway between the network and the internet. This operation is shown in figure 1.4, extracted from [8]. Despite some limitations (like relatively short battery life), this system shows the possibility of remote real-time monitoring, overcoming the difficulty due to the lack of communication systems in certain areas.

Figure 1.4: Data collection from sensors in a vineyard with a remote wake up device (drone).

Chapter 2

Energy harvesting sensor nodes

WSNs are meant to provide continuous monitoring of the physical world; thus, the main challenge is to extend the lifetime of the nodes so that they can operate autonomously for long periods. In general, these devices are powered by batteries, which require regular human intervention to replace or recharge them, not considering the high polluting level of exhausted batteries. The use of large batteries to prolong the lifetime also poses the problem of higher cost and bigger size. The network's performance is critically compromised if one node runs out of battery and gets isolated from the others.
Energy harvesting is one of the most promising techniques that has been proposed so far to address the issue of finite energy supply. Nodes can replenish their energy by harvesting it from the environment and converting it into electrical energy. Doing this, they can theoretically operate for an unlimited length of time, eliminating the problem of replacing exhausted batteries, which could be difficult or even impossible in certain environmental conditions. When the performance is maximized according to the available energy and the depletion of energy never occurs, the operating mode of the harvesting node is called energy-neutral operation [14]. This result can be obtained by tuning the system parameters dynamically according to the expected output energy that can be extracted from the environment.
According to [14] an energy harvesting system consists of three components: an energy source, a harvesting architecture, and a load. The first refers to the source of energy to be harvested and will be treated more specifically in the following section. The harvesting architecture refers to the technology to extract ambient energy and convert it into electrical energy. In many cases, the available excess of energy with respect to the one currently used is stored in a storage element that is also used to power the node later when harvesting opportunities decrease or are

absent. Load refers to the energy-consuming activity. The activity of a typical load is variable in time, as in the case of a sensor node that has different instantaneous power consumption when sampling the sensor or transmitting data. This leads, in most cases, to the use of a power management strategy to adapt the variable energy generation profile to the variable energy consumption profile of the load.

2.1 Energy sources

Thanks to the significant improvement of the energy harvesting technologies, there is a wide choice of sources from which the energy needed to power the electronic devices used for environmental monitoring can be extracted. These are typically classified into two categories: ambient sources of energy, such as sun, water flow, wind, RF and vibration, and man-made energy sources, like human walking.
Usually, designers have no control over the ambient energy output since this depends on the environmental conditions that are variable in time, but they can predict it, as for solar energy, which has a known behavior within days and seasons. Many commercial harvesters exploit this energy source since it is renewable, easily available, reliable, and presents high power density.
In literature, there is plenty of examples of solar-powered monitoring systems. Authors in [15] presented a system deployed in Australia to monitor the underwater temperature and luminosity that uses poly-crystalline solar cells to power both the sensor nodes and the gateway. The energy harvesting unit includes an MPPT (Maximum Power Point Tracking) circuit, which ensures that the output voltage of the cells is around the peak of produced power. The storage element is constituted by two battery packs performing full charge and full discharge cycles to overcome the reduction of the battery's nominal capacity caused by partial charge/discharge cycles. The energy harvesting system presented in [16] is designed to power WSNs for the IoT. Whenever the sun is shining, and so the harvested energy is sufficient to satisfy the load power requirements, it exploits the power extracted through a solar panel, while, when the illumination is not enough (during the night, in case of rain, etc.), the system is powered by the energy stored in a lithium battery. As the harvester presented above, this application exploits an MPPT circuit to provide the system with the maximum power produced by the solar panel.
The source of energy exploited in the sensing application proposed in [17] is instead environmental vibration. As underlined in the document, powering a system through vibration requires using a high capacity storage unit since this source is variable, both in amplitude and duration, and unpredictable. In the paper, vibration energy is extracted from the ambient using two different harvesters: a piezoelectric one, stimulated through a shaker table, and an electromagnetic one

attached to the wrist of a runner. The system can achieve energy-neutral operation thanks to the development of a node that is self-adaptable: depending on the energy availability and the power required for a given task, it can autonomously change its duty-cycle, enhancing the lifetime.
Wind is instead usually used as energy source mostly with large-scale harvesting systems for high power applications. Nevertheless, the authors in [18] managed to develop a small-scale harvester overcoming the issue of low output voltage that typically affects these types of systems, thanks to the use of an efficient power management unit. The MPPT operation, which ensures that the maximum power is harvested from the generator, is performed through a resistor-emulation approach: the effective resistance of the load can be dynamically changed in order to match the internal resistance of the microwind turbine generator.

2.1.1 Biomass as a source of energy

An emergent alternative for the production of sustainable energy is represented by PMFCs (Plant Microbial Fuel Cells). This green technology takes advantage of solar energy, a renewable and reliable energy source, and converts the biomass produced by it into bioelectricity, exploiting the metabolism of the organisms living at the plant's roots.
As explained in [19] many are the advantages of PMFCs over the other systems currently used to extract bioelectricity from a biodegradable substrate. Considering the extreme pressure on Earth's vegetated lands analyzed in the first chapter, of primary importance is that this technology, unlike many other biomass energy technologies, does not need landscape transformation and is not competitive with arable lands needed for food production. Next to this, the conversion of a biodegradable substrate into bioenergy is achieved in situ (so the plant does not need to be harvested) and without energy-intensive processes that are instead typically required by this type of system since they exploit high temperatures and combustion. An overview of the basic technology (Microbial Fuel Cell) from which PMFC has been developed will be given in the next section.

2.2 Microbial Fuel Cell

Since the early 19th century, it has been known that microbes release electrical energy during the disintegration of organic matter. The first demonstration of a MFC (Microbial Fuel Cell) from 1911 can be found in [20], where Professor Potter managed to collect and deliver to a condenser the electrons liberated during the living cultures' vital processes through the use of platinum electrodes employed in a

galvanic cell. Later on, this technology has gained attention from researchers since, in the 1980s, it was found that the addition of electron mediators could enhance the output power and the current density [21]. Then, in 1991, the treatment of wastewater through the use of MFCs was considered. However, only in the last decades, the developed MFCs were able to produce an enhanced output power that made them suitable for practical applications.
In a MFC, the microbes, separated from any terminal electron acceptor (like oxygen) at the cathode, transform chemical energy into electrical energy during the degradation of an organic substrate. Any biodegradable material can be used as the substrate for electricity generation: pure compounds (such as ethanol, acetate, glucose, etc.) or complex mixtures of organics present in wastewater and plant rhizodeposits.
The wide choice of configurations and the big variety of materials that can be used in the design of a MFC is reviewed in document [22] and in document [21]. A traditional design is the two-chamber MFC, illustrated in figure 2.1, taken from [21]. This configuration was widely used for research scopes when the interest in this technology increased in the early 2000s.

2.2.1 MFC operating principle

Micro-organisms oxidize the organic matter or wastewater with which the anodic chamber of the electrochemical fuel cell is fed, releasing electrons and protons. The generated electrons are not absorbed by oxygen (natural electron acceptor) since the chamber is anaerobic, but by the cell anode (negative terminal) and then flow, through a resistor (or a load), to the cathode (positive terminal) where the available electron acceptors are reduced. This generates an electric current that can be considered positive, by convention, flowing from the cathode to the anode. A number of protons equal to the number of electrons move to the cathodic chamber through a proton exchange membrane (PEM) (also called cation exchange membrane). At the cathode, protons react with electrons and oxygen (O_2) provided by air, forming water.
The membrane must allow protons to pass towards the cathode, but not oxygen or other electron acceptors to move to the anodic chamber. The presence of a PEM is not strictly needed, and many are the examples in the literature of membrane-less MFC. Authors in [23] present a mediator-less and membrane-less MFC, used for wastewater treatment together with electricity production. A not efficient proton transfer to the cathode can limit the operation of a cell if the membrane permeability is poor. Thus, the membrane removal enhances the performance, also eliminating part of the cost.
The product of the microbially catalyzed oxidation is carbon dioxide, but this can not be considered a net carbon emission since the biodegradable substrate contains

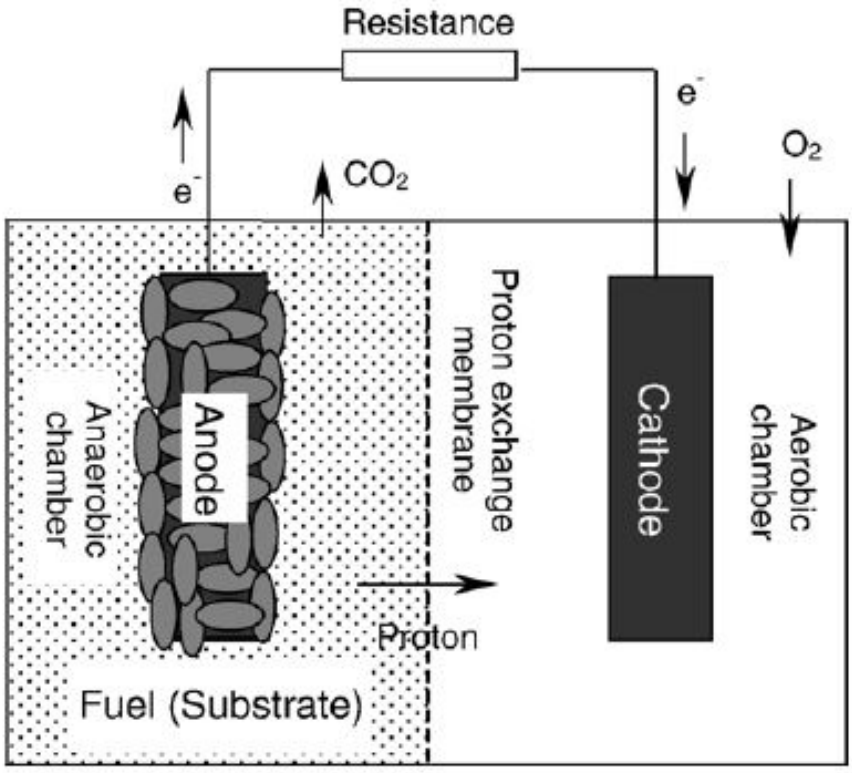

Figure 2.1: Two-chamber MFC model. Due to the potential difference, electrons flow from the anode to the cathode through an external resistance generating electricity, while protons move across the PEM towards the cathode. CO_2 is released as a product of the anodic oxidation, while oxygen is reduced at the cathode.

CO_2 that is absorbed originally from the atmosphere with photosynthesis. The two typical reactions at the anode, where acetate (CH_3COO^-) is considered as substrate example, and at the cathode of the microbial fuel cell are the following (extracted from [21]):

- Anodic reaction catalyzed by microbes (oxidation):

$$CH_3COO^- + H_2O \longrightarrow 2CO_2 + 7H^+ + 8e^-$$

- Cathodic reaction (reduction):

$$O_2 + 4e^- + 4H^+ \longrightarrow 2H_2O$$

The net balance of these reactions is the breaking down of the substrate and the production of CO_2 and H_2O, with electricity being produced as a by-product.

The cell voltage is given by the difference of the two electrodes' redox potential.

2.2.2 Anodic electron transfer mechanisms

As stated by the authors in [24], until almost the end of the last century, it was believed that an acceptable amount of power could be generated in a microbial fuel cell only through the addition of exogenous mediators. Indeed, electrons need a physical transport system to be delivered towards the anode. However, now it is known that the presence of external mediators is not necessarily needed, but only if the involved microbes are not able to transfer electrons directly to the electrode. Three are the possible mechanisms of electron transfer to the anode:

- *Mediated electron transfer*: The majority of the microbial communities are composed in the outer layer of non-conductive lipid membranes and, therefore, they are incapable of direct electron transfer. In these cases, external redox mediators, which can be natural or artificial, are responsible for the extracellular transfer and influence the cell performances. They capture electrons from a cellular compound (within the cell membrane), oxidizing it, and, moving through the membrane, they release the electrons to the electrode surface, becoming again oxidized [21]. Bacteria can also use some naturally available compounds as mediators, like the metabolites produced by the same microbes.
- *Direct electron transfer*: Among the bacteria species, there are some electrochemically active species capable of transferring electrons directly to the electrode. These microbes form a biofilm on the anode surface and, using the electrode as the final acceptor during the anaerobic respiration, transfer the electrons through the membrane by conductance. Mediator-less MFCs are convenient since the mediators' cost, which is usually high, is eliminated and also because mediators are generally toxic.
- *Transfer through nanowires*: As widely explained in [24], some bacteria families produce electrically conductive nanowires (pili) that allow the extracellular transfer of electrons to the anode even if the cell is not directly in contact with the electrode surface.

2.3 Plant Microbial Fuel Cell

Obtaining energy starting from waste through a biological process make MFCs an appealing alternative for sustainable energy. Many are the applications of these cells: besides being used for bioelectricity production, they have been used as biosensors, for wastewater treatment, and for hydrogen gas production. Many are

also the modifications that have been applied to the MFC during the years, and today many descendants of the primary cell can be found in the literature, such as sediment-MFC and constructed wetlands-MFC.
Among them, the one considered in this work is the plant-MFC: a biological cell where a plant is incorporated at the anode region of a microbial fuel cell to provide the organic substrate for bacteria. The cell acts as a biosystem, and it is based on two processes: the transformation of solar energy into rhizodeposits thanks to the photosynthetic process of living plants and the subsequent transformation of these organics in bioelectricity by micro-organisms. This unique relationship between microbes and plants enhances the output power with respect to a simple MFC since the plant continuously provides nutrients to microbes.
Indeed, during their living life, plants undergo the process of photosynthesis, where, fixing CO_2 through the use of a pigment present in their leaves called chlorophyll, they produce biomass. According to [25], up to 60% of this organic matter is lost and transferred to the soil with roots exudation. This process, called rhizodeposition, is the source of many organic compounds in the soil. The rhizodeposits act as the fuel for the microbial fuel cell since the micro-organisms metabolize the organic carbon contained in the substrate, mainly glucose.
To achieve the optimal operating condition of a PMFC, the maximization of photosynthetic activity with consequent maximization of roots exudates is essential as the optimization of the microbial community conditions. The plant status affects the performance of a PMFC since it affects the condition of the surrounding soil. Since bioelectricity is produced in situ, nutrients are preserved in the soil, and the biomass does not need to be transported: these are two fundamental advantages of a PMFC with respect to other ways of producing bioenergy.

2.3.1 The role of bacteria

Bacteria use the chemical energy contained in the bioconvertible substrate for their metabolism and thus avoid losing a big part of the solar energy captured by plants as rhizodeposition in the soil. Next to exploiting this true green energy, otherwise lost, this process reduces the emission of methane, a greenhouse gas that represents one of the most effective in causing global climate warming.
The issue of methane emissions is evident in wetlands, including ones constructed for rice agriculture, that emit yearly 82% of methane emitted naturally on Earth [26]. The electrogens that generate current in a MFC reduce, decomposing part of it the quantity of organic carbon available in the soil. As widely explained in [27], methanogens have therefore limited possibility of anaerobically degrading carbon, and so the emissions of methane are significantly lowered if MFCs are employed in constructed wetlands.

In a PMFC, the process at the base of electricity production happens at the anode region, where the plant roots are integrated, and so a big concentration of bacteria is present. Authors in [28] explain the three possible metabolic pathways, depending on the anode potential, of microbial populations, corresponding to three different flows of electrons and, concomitantly, protons.
The first way is used by bacteria when the anodic potential is high (high redox oxidative metabolism) and can not be used in a PMFC. Indeed, bacteria exploit the respiratory chain to metabolize nutrients and, since various inhibitors are present in this chain, an electric current can not be generated. Another type of oxidative metabolism is used by microbes when the anode potential is reduced (medium to low redox) and electrons are deposited onto natural acceptors present in the region. Electricity generation is achieved only in the third metabolic pathway: when the potential of the anode remains low and the natural acceptors, like nitrate, sulphate, and oxygen, are not present. In this case, fermentation is the way of metabolism used by rhizosphere bacteria. Electrons are transferred to the anode of the cell, an insoluble acceptor that becomes the preferred one [28]. Therefore, it is important to study the wide range of microbial communities to understand better the operation of a PMFC and how to achieve maximum power densities.

2.3.2 PMFCs review

The concept of PMFCs was introduced in 2008, and it has been developed during the years with the priority of harvesting enough energy in environmental applications from the unlimited amount of fuel that the nature offers so that this technology can be used to power wireless sensor nodes for the IoT.

In 2008, the authors in [19] presented the concept of producing green electricity through a PMFC without competing with currently used bioenergy systems but expanding them and demonstrated its feasibility. The experimental set-up consisted of a glass tube as anode compartment and a baker glass as cathode compartment. For the two electrodes, graphite felt was used as the conductive material. The two compartments were separated by a cation exchange membrane. The anode compartment, in which a stem of *reed mannagrass* was placed, was inoculated with active bacteria from another MFC to enhance the presence of micro-organisms with respect to the naturally occurring communities.
The cell was illuminated artificially with a light intensity of 15 W/m^2 and the cell voltage was monitored for 118 days. The conditions appropriate to produce electricity were obtained after an incubation period of 50 days, after which the voltage increased, reaching a maximum of 253 mV. The internal resistance, determined using the electrochemical impedance spectrometry (EIS), was found to

be high with respect to simple microbial fuel cells, indicating that the electrical output can be enhanced by improving the design of the cell, as well as improving the plant selection and the management if its vitality. Indeed, in the experiment, the plant health status declined after day 68; this clearly compromised the release of nutrients from the roots and, therefore, energy production.

The internal resistance must be decreased to improve the electrical output of a PMFC: this is widely treated in [29], where the authors propose a flat-plate design. This choice aims to reduce the distance between the two electrodes with respect to the tabular design utilized in the PMFC presented in [19]. This is done to reduce the proton transport distance from the anode to the cathode and so the transport resistance, which affects the internal resistance significantly. In the flat-plate design, the cation exchange membrane is placed vertically between anode and cathode, which are located one next to each other so that the protons produced at the anode region have to travel a shorter distance to reach the cathode, as clearly shown in figure 2.2 (extracted from [29]), which compare this design with the tabular one.
In order to evaluate the internal resistance at various depths, three different anodes, electrically not connected, were placed in the cell, and the electrical characteristics were measured for 350 days. This configuration allowed the authors to demonstrate that the presence of the plant's roots boost the production of electricity since the top anode, where most of the roots are located, showed the best performances among the three anodes.
The authors did not manage to obtain a lower total internal resistance of the cell since, even lowering the transport resistance, other partial internal resistances contribute to this parameter, as the anodic resistance, which is higher than in the tabular PMFC. However, this system allowed to obtain higher current and power densities normalized to plant growth area with respect to the previously presented designs.

In recent years, the power extracted from a PMFC has reached levels high enough to allow the realization in smart farming applications of WSNs that are self-autonomous thanks to the energy harvesting through this technology. An example can be found in [30], where the authors present an energy-neutral system where the PMFC is used not only to power the wireless embedded electronics but also as a biosensor to monitor the plant health status. Indeed, the PMFC performances are correlated (among several other factors) to the conditions of the surrounding soil and, in turn, to the plant status.
The schematic representation of the cell is shown in figure 2.3 (extracted from [31]). It is composed of two electrodes made out of graphite fiber. The cathode is placed at the top of the plastic can (which is fed with soil) so that it is exposed to oxygen (which reacts with protons and electrons, giving water as a by-product).

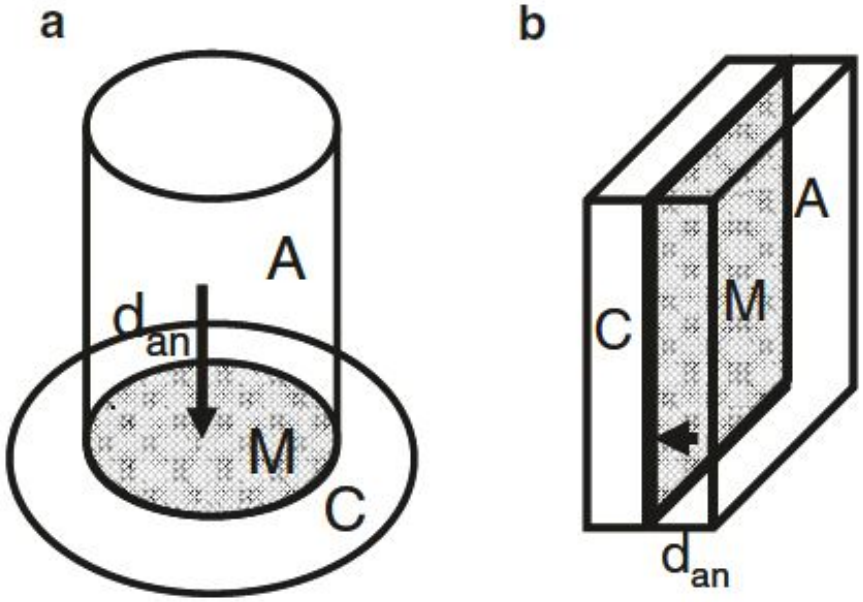

Figure 2.2: Tabular (a) and flat-plate (b) PMFC designs. A = anode, M = membrane, C = cathode, d_{an} = distance between anode and membrane.

The anode is instead placed at the bottom since it must be, as already explained, in an anaerobic compartment. In this configuration, the proton exchange membrane is not needed since the processes of reduction and oxidation at the two electrodes are separated by the soil in between them, which acts as a membrane.
The whole electronic unit, which comprises a light sensor to monitor environmental conditions, is ultra-low power (average consumption of few μW), and it can be turned off for long sleep intervals when it does not need to do the measurements and send the data through the radio component. In the experiment, the cell, through a DC-DC boost converter that implements an MPPT algorithm, was able to recharge a 10 mF supercapacitor in just five minutes, allowing an unlimited operation of the monitoring system. The possibility for long-term flora health assessment through the cell output was demonstrated by the fact that the generated maximum power increased together with the plant growth, reaching 300 μW with a load of 800 Ω.

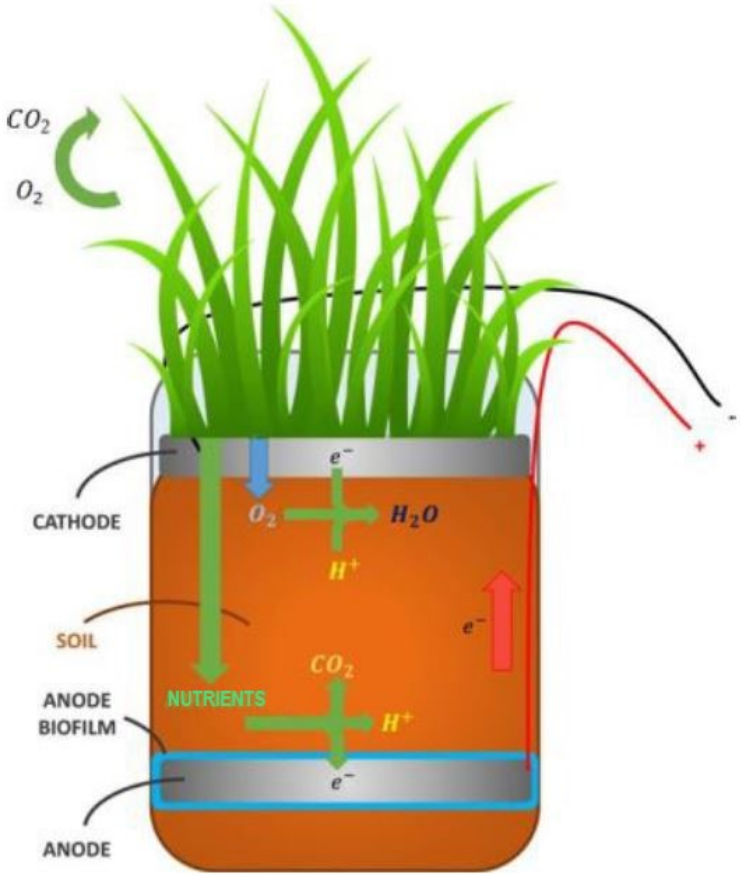

Figure 2.3: Schematic representation of the PMFC and of the reactions that take place at the anode and at the cathode.

Authors in [32] present another example of self-powered PMFC-based wireless sensor node for the IoT. The system, used to monitor environmental conditions in agricultural applications (i.e. temperature and humidity), comprises a nano-power boost converter to overcome the very low input voltage, a typical issue of this type of energy harvesting system. A dynamic power management technique is adopted to reduce the consumption of the ultra-low-power electronic unit by dynamically switching the components to low-power modes. Indeed, the behavior of environmental parameters (among which temperature and humidity) is typically quasi-static during the day, so it is not necessary to collect data frequently. This allows to drastically reduce the average consumption compensating for the slightly higher energy demand of the data transmission state with long intervals of sleep state, which present a very low current consumption.
The design of the cell, illustrated in picture 2.4 (extracted from [32]), differs from

the one adopted in [30] for the position of the cathode, which is placed at the bottom of the pot instead of being placed at the top of it. The authors demonstrated that the performance of the PMFC is enhanced (several orders of magnitude) using a zinc mesh anode and a spiral copper cathode rather than electrodes made out of stainless steel. The constructed cell is depicted in figure 2.5 together with the energy harvesting system (DC/DC converter and supercapacitors), the sensor node system (data acquisition and signal conditioning module, MCU and wireless transmission module), and the SHT10 temperature sensor. With this configuration, the PMFC reached a power output of 3.5 mW/cm^2, which, considering the sensor node average power consumption of slightly more than 1 mW, was sufficient to sustain the autonomous operation of the node.

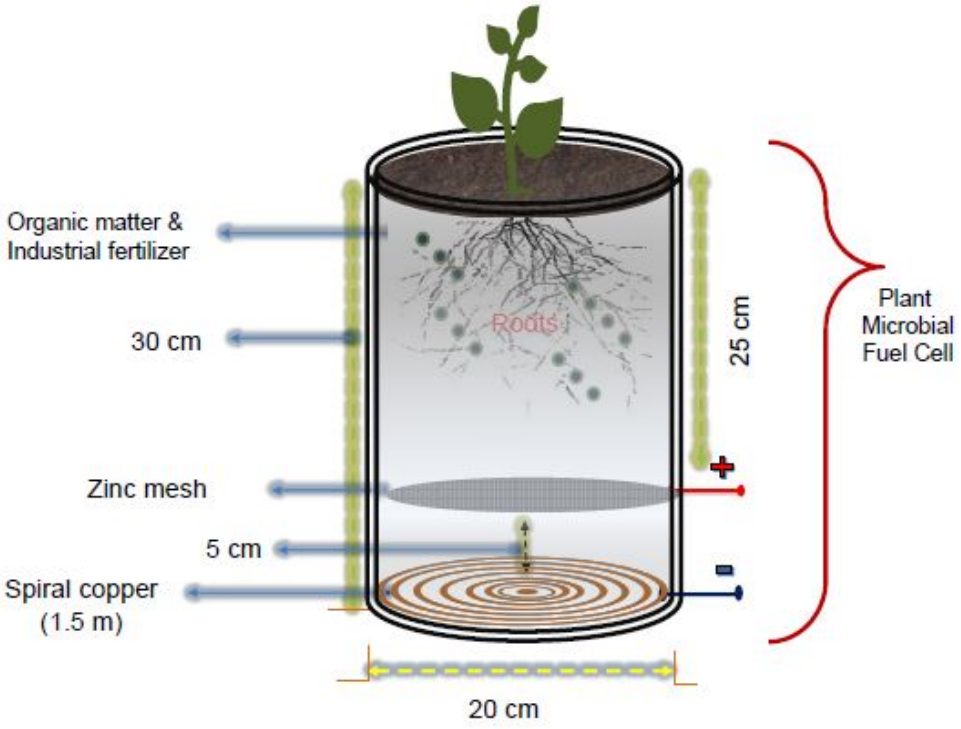

Figure 2.4: Set-up of the designed PMFC. The electrodes are placed in a plastic pot filled with soil enriched with industrial fertilizer, with the cathode at the bottom and the anode in the rizhosphere region (5 cm above the cathode).

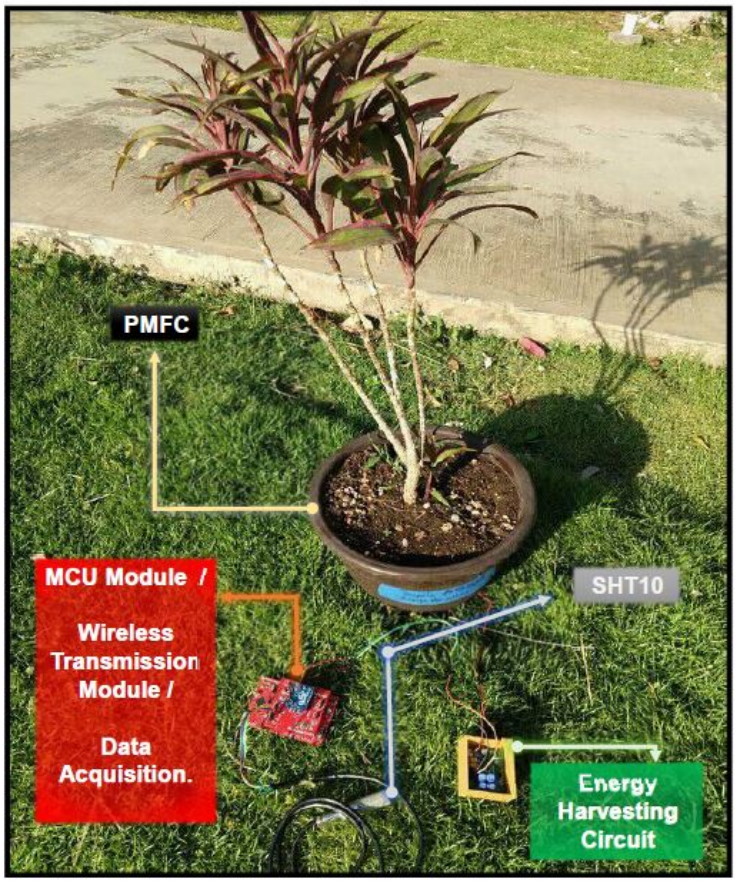

Figure 2.5: PMFC-based energy harvesting system.

Paper [33] presents a PMFC-based energy harvesting system that can sustain the operation of a wireless sensor node, together with an exhaustive analysis of the energy required by the sensor node to send a certain amount of data in order to estimate the lifetime of the system. The design of the cell is presented in figure 2.6 (extracted from [33]) and consists, as in the previously presented document, of a copper cathode and a zinc mesh anode, but placed in a different configuration, with the cathode forming a helix in the plastic pot, as can be observed in the figure, and the anode at the bottom of the plastic pot.

The cell, which collects energy from plant *Mentha piperita L.* (peppermint or mint), allows the system to never run out of energy. This is obtained thanks to the dynamic switching ON and OFF of the nodes: when a node is in sleep state, the supercapacitor can be recharged with the harvested energy, while, when the node must send some data, it wakes up and uses part of the energy stored in the supercapacitor.

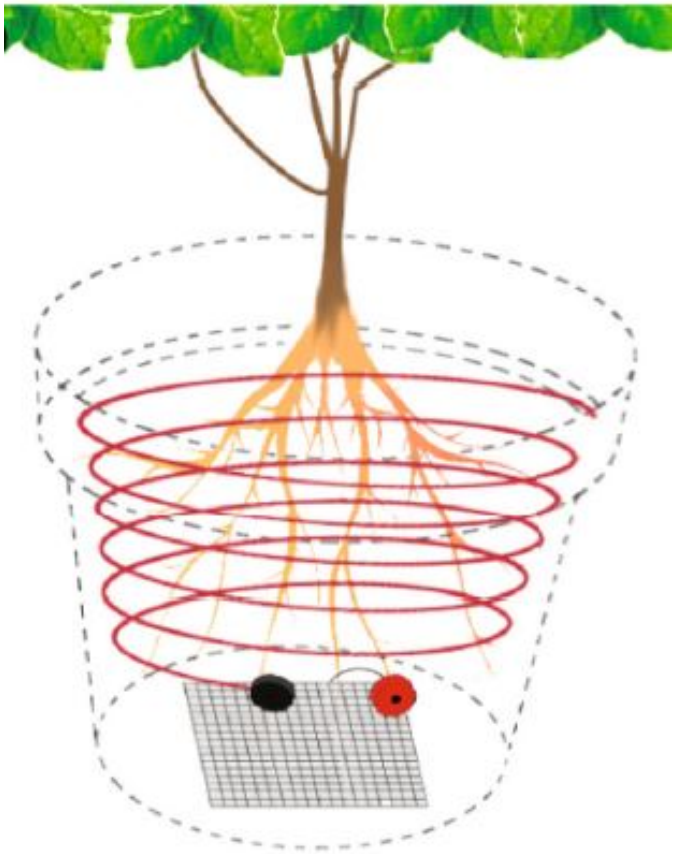

Figure 2.6: PMFC set-up with a 7-turn copper wire helix as cathode (inside which the mint plant roots are placed) and a zinc-plated wire mesh as anode.

The selection of a suitable plant is important to maximize the performance of the harvesting system. As widely treated in [25], depending on the photosynthetic activity, plants can be classified into three categories: C3, C4, and CAM. C4 plants have a theoretical higher photosynthetic efficiency, which means a higher conversion rate of light into bioelectricity with respect to the other classes of plants. C3 plants (among which mint can be placed) have a reduced photosynthetic activity since they dissipate part of the energy for photorespiration, an important process to mitigate the effect of dry and hot conditions. According to paper [25], since many are the parameters that influence the performance of the cell, the effect of the photosynthetic activity on the cell performance is not easily understandable, and it must be investigated further, but in most of the analyzed cases plants belonging to C4 class allowed to obtain higher power output.

A serial-parallel array of PMFCs is implemented in paper [34] to sustain the operation of a wireless sensor node that comprises a piezo-resistive pressure sensor. The harvesting system uses a power management subsystem that manages the storage of the harvested energy in the supercapacitor. When there is enough accumulated energy, it can be used to power the node, ensuring the self-sustainable operation of the WSN. Analyzing the cell for 30 days, the authors obtained a daily energy generation of about 85 J, much greater than the node's energy requirement. In this study, each of the cells constituting the array was implemented in a plastic cylinder with the same electrodes employed in [32], but with the position switched.

Chapter 3

PMFC design and operation

The plant selected for the cell is tobacco (*Nicotiana tabacum L.*). This perennial herbaceous plant belongs to class C3 since the first product of photosynthesis (CO_2 fixation) is a three-carbon compound [33]. The choice of this plant is due to the availability of grown crops used in other studies in the laboratory where the experiment has been set up. In these studies, tobacco was selected since it is among the plant species whose genome has been completely sequenced. Moreover, it is very easy to grow tobacco plants, even in a closed environment as the laboratory. It is thus possible to obtain many specimens to perform real tests.

Figure 3.1 shows a schematic representation of the proposed PMFC. A plastic pot with a height of 50 cm and a diameter of 54 cm was filled with soil, which was enriched, in the first five days of the experimental set-up, with industrial fertilizer to enhance the presence of nutrients in the soil (1l of water with fertilizer per day). The fertilizers used were B'cuzz Soil A and B'cuzz soil B (3 ml A and 3 ml B per liter of water), which have the following compositions:

- B'cuzz Soil A: 3.2% N, 3.0% NS, 0.2% NA, 3.2% K_2O, 2.6% CaO, 0.03% Fe
- B'cuzz Soil B: 2.9% P_2O_5, 4.3% K_2O, 0.02% Mn, 0.001% Mo, 0.03% Zn

The cathode is a 1 mm diameter copper wire of 150 cm. The wire forms a spiral with a diameter of 20 cm (figure 3.2). It is placed at the bottom of the container, just above a thin layer of soil. A zinc-plated wire mesh (figure 3.3) placed 5 cm above the cathode constitutes the anode. As can be observed in figure 3.3, three layers of wire meshes were overlapped and fixed with two bolts to increase the surface where the reaction can happen since a mesh with a smaller size was not available. The choice of these electrodes was suggested by the good results obtained with this combination (Cu/Zn) in many of the mentioned papers ([32], [33], [34]). The anode was covered with other 20 cm of organic soil, and some medium-size

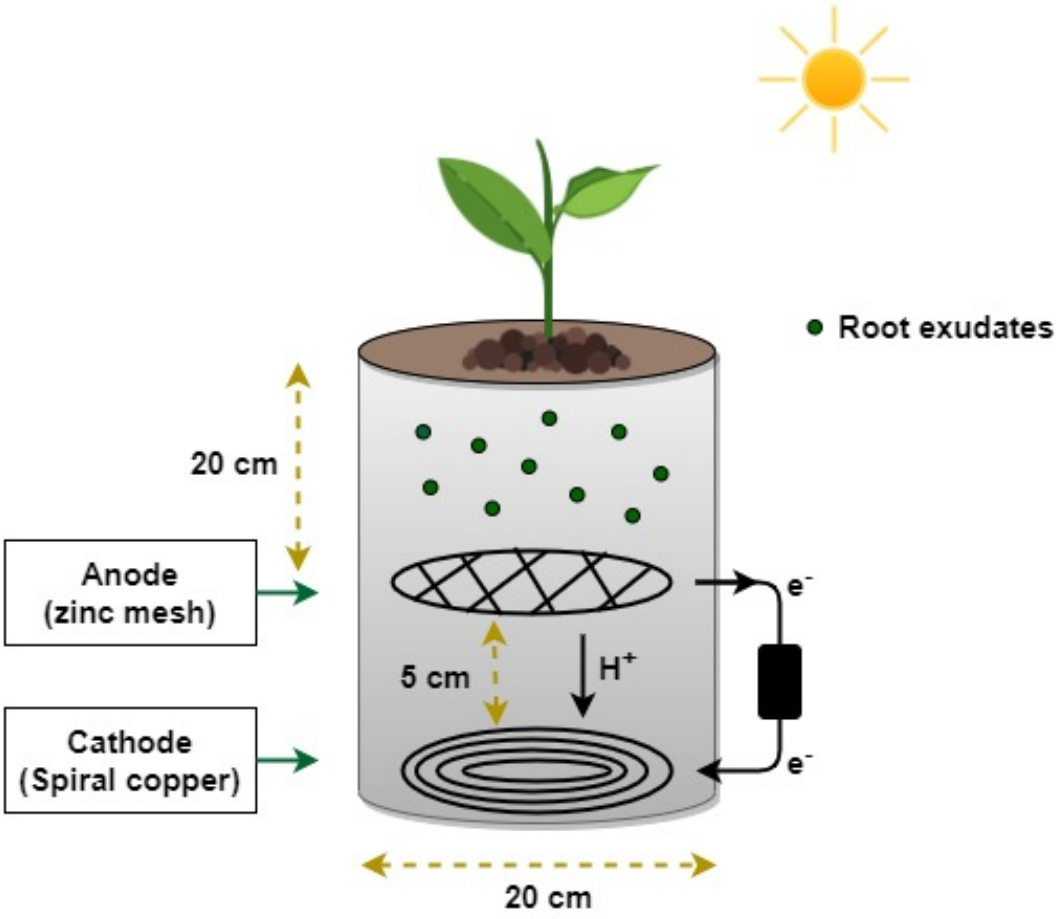

Figure 3.1: Schematic design of the proposed PMFC. A plastic container filled with soil into which tobacco plants are placed. The electrodes in the plastic pot are separated by 5 cm of soil. Electrons flow from the anode to the cathode through the external load, while protons move through the soil towards the cathode.

tobacco plants were placed above it. Two copper wires were connected to the electrodes and brought outside the pot through a small hole performed in the container to connect the external circuit. The protons released in the oxidation of the organic sources at the anode move to the cathode through the soil that separates the electrodes, which acts as the proton exchange membrane. The cell was placed indoors next to a south-facing window, with good natural illumination during all day. The real set-up of the implemented PMFC can be observed in picture 3.4.

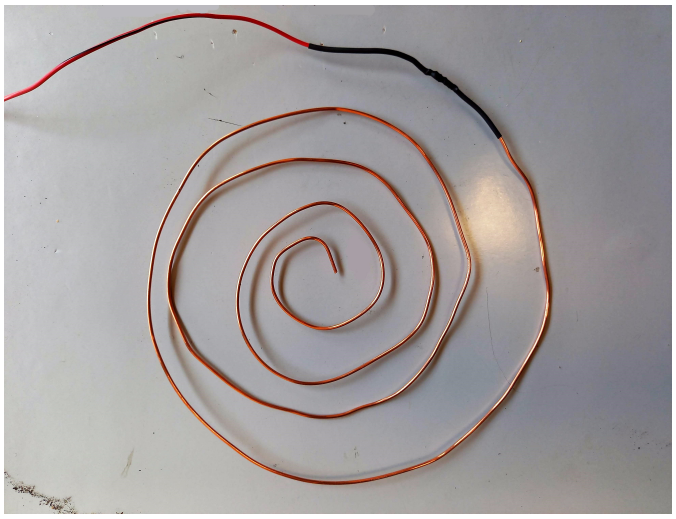

Figure 3.2: 1 mm diameter spiral copper anode.

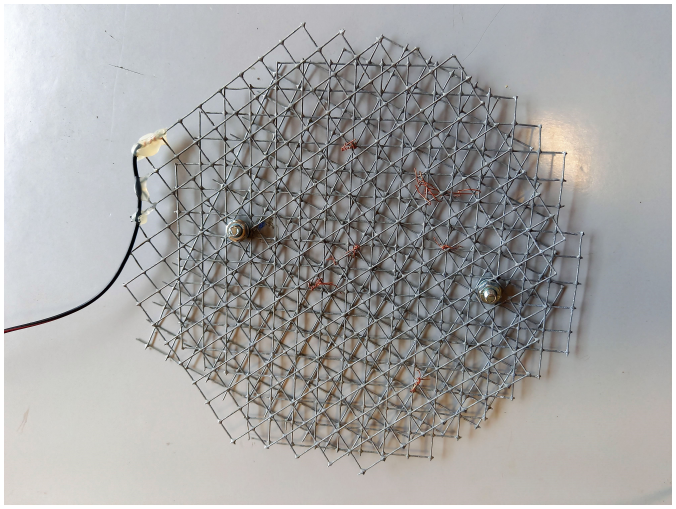

Figure 3.3: Zinc-plated wire mesh cathode.

Figure 3.4: Picture of the implemented PMFC.

3.1 Cell characterization

The implemented PMFC performance (deliverable power levels) has been evaluated through the cell characterizations presented in this section.

3.1.1 First cell characterization

The cell was characterized for the first time after five days from the day the cell was built. The cell was loaded with a resistive load changed manually in a range from 1 Ω to 1 MΩ. The voltage across the resistance was measured with the digital bench-type multimeter 34401A from Agilent Technologies. The results are shown in figure 3.5. From this characteristic, it is possible to evaluate the maximum power

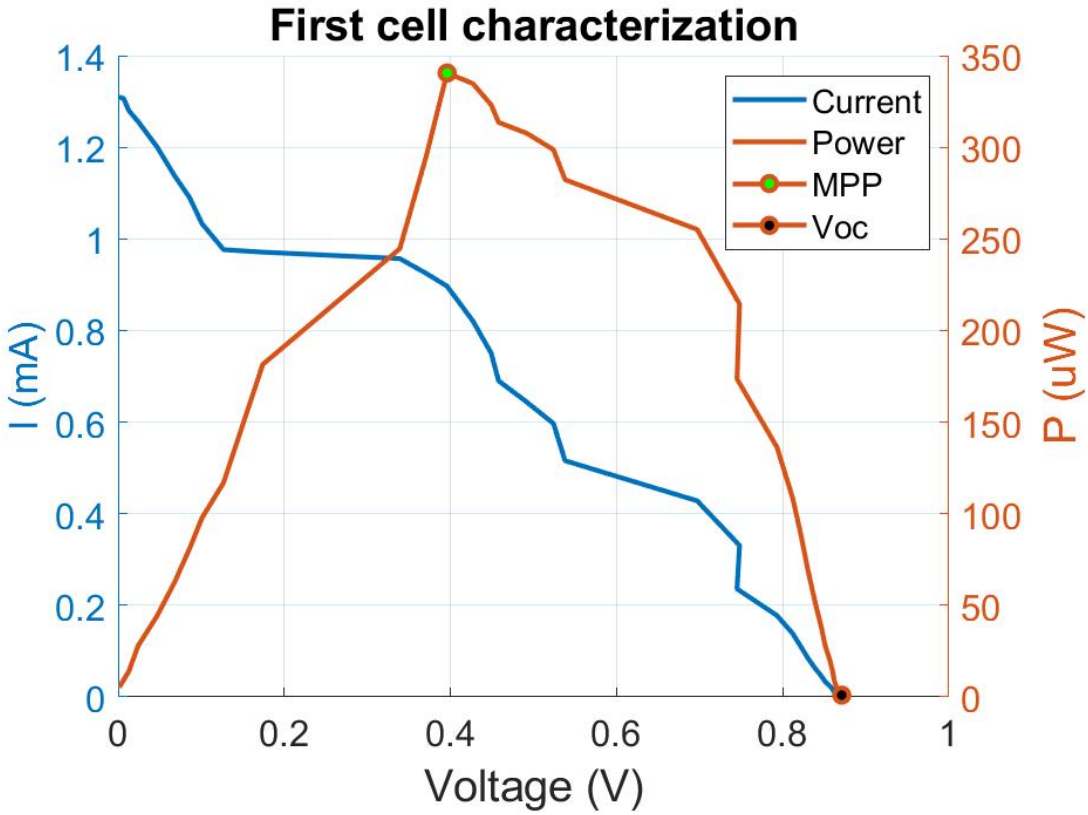

Figure 3.5: Cell characterization carried out measuring the output voltage across a resistive load (1 Ω to 1 MΩ).

point (MPP). It is important to know this parameter when working with all the sources that give a variable power output. Indeed, it allows maximizing through a maximum power point tracking (MPPT) algorithm, in any condition, the energy

extraction. As can be observed, the MPP occurs at a voltage $V_{MPP} = 0.396$ V, where the cell output power is 340.58 μW. The open circuit voltage (V_{OC}) and the short circuit current (I_{SC}) were measured with a digital multimeter as well, and the obtained value were $V_{OC} = 0.871$ V (marked with a black dot in picture 3.5) and $I_{SC} = 1.3$ mA. From these values it was found out that $V_{MPP} \simeq 0.45 \cdot V_{OC}$.

3.1.2 Second cell characterization

The performances of the cell were evaluated again 88 days after the first characterization. The results obtained, shown in figure 3.6, were not satisfactory. Indeed, the PMFC output current and power resulted to be about two orders of magnitude lower, with a maximum power of 7.11 μW.

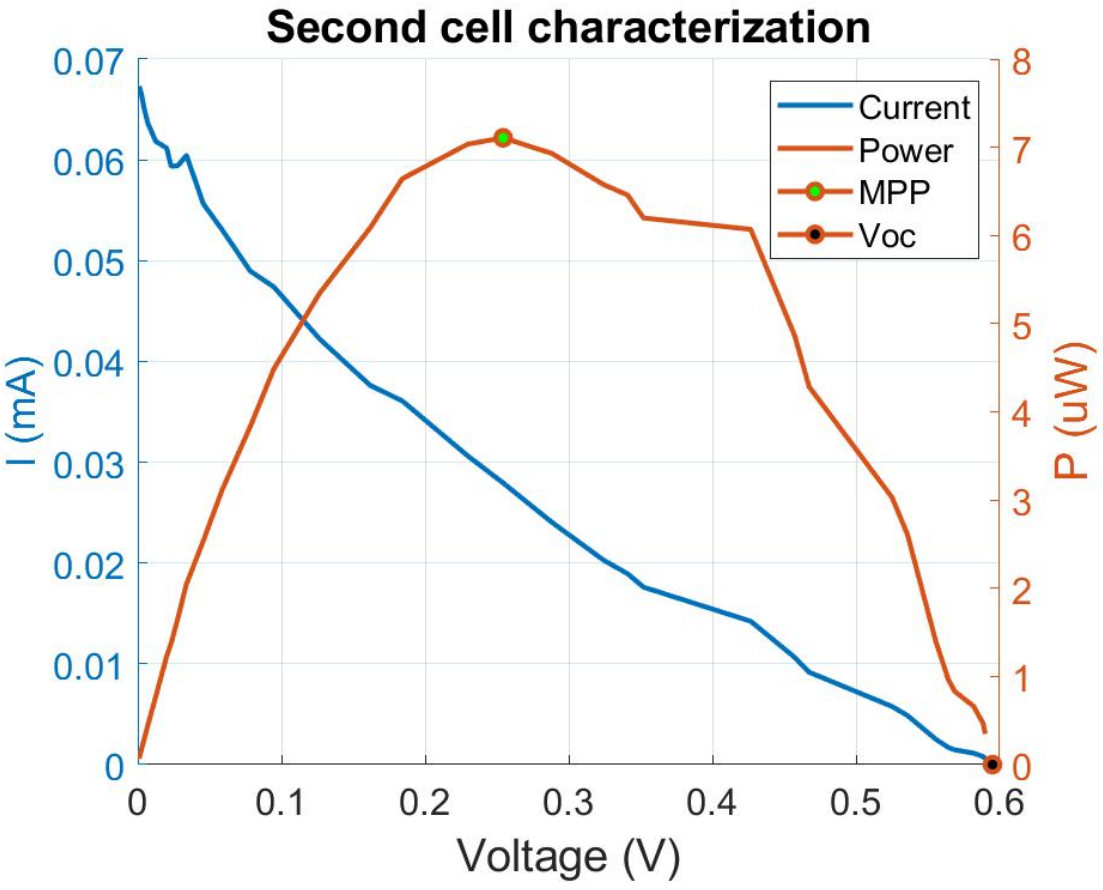

Figure 3.6: Cell characterization repeated after 88 days from the first one.

3.1.3 Third cell characterization

The first hypothesis about the reduction of the electrical characteristic was that the electrodes, buried in the soil inside the pot, degraded getting oxidized. No other hypotheses were considered since the plants were grown and in good health status, and the change of season (from summer, when the cell was built, to autumn) should not influence the production of bioelectricity in this type of harvesting system. In order to verify the status of the electrodes, the plants were removed from the container to extract the electrodes from the soil. The cell was then set up again with new copper and zinc electrodes and with the same tobacco plants and soil.
The cell was characterized again. It showed good results, similar to those obtained from the first characterization, which means the degradation of the electrodes was the reason for the reduced performances. The output current and power given by the cell are shown in figure 3.7. The open circuit voltage was very similar to the first one, with a value $V_{OC} = 0.878$ V, while the short circuit current increased slightly, reaching $I_{SC} = 1.8$ mA. The value of maximum power extracted from the cell was 275.3 μW, in correspondence of a voltage $V_{MPP} = 0.301$ V, which represents about the 35% of V_{OC}.

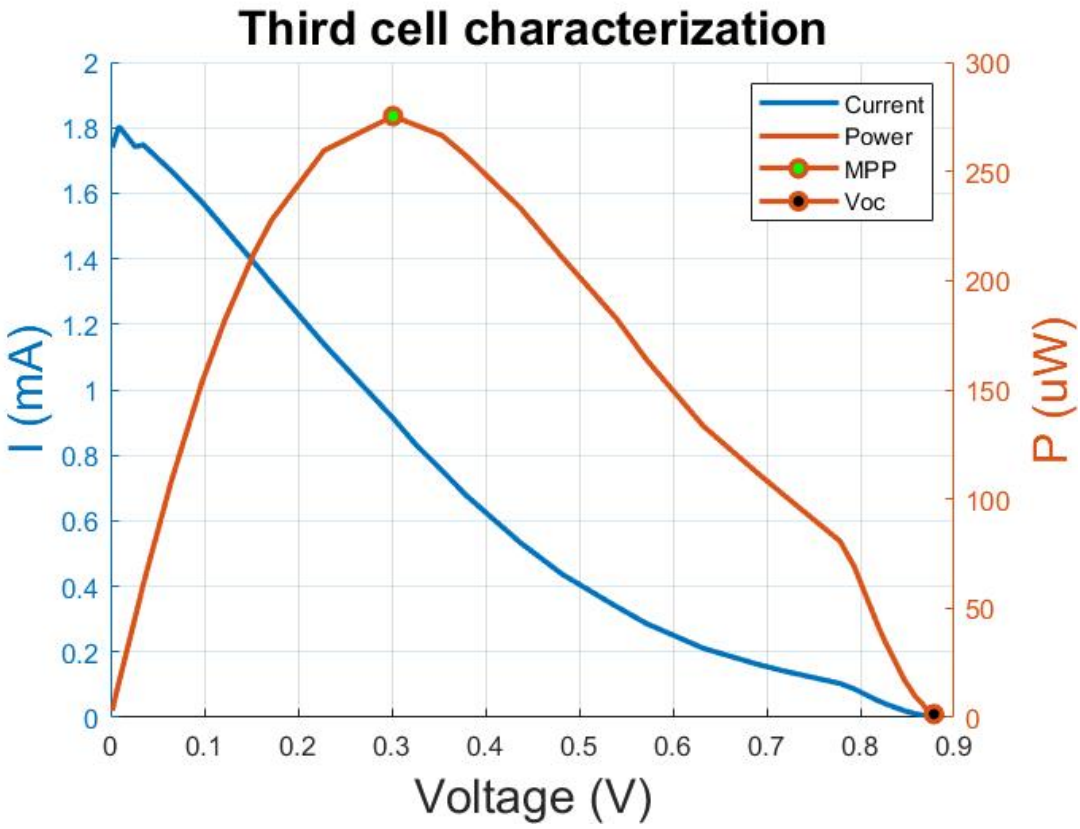

Figure 3.7: Cell characterization after the electrodes were changed.

Chapter 4

System architecture

4.1 Plant monitoring system

The energy extracted from the PMFC is used to sustain the autonomous operation of a receiving subsystem, which is part of a plant monitoring system. This latter is a sensor node to inspect the health status of crops having as objective the optimization of the water use and the planning of the irrigation events, and it is based on the in-vivo measurements of the plant stem impedance. Indeed, many of the monitoring systems presented until now rely on the data collection of the environmental parameters (illumination, soil moisture, humidity, etc.) affecting the plant health and not on the direct inspection of the latter.
The idea on which is based the monitoring system presented here comes from the study carried out in paper [35], where the authors measured the plants' electrical impedance to correlate the gathered data to the watering events. It was observed that the soil moisture changes affect the impedance modulus.
Thus the present monitoring system inspects the plant status (drying process) by measuring its electrical impedance. The possibility of using a green plant stem to transmit an electrical has been demonstrated in [36]. Indeed, the authors managed to set up an electrical communication inside the body of a *Prunus Bianco* through galvanic coupling.
The concept of using the plant stem as a communication channel is exploited together with the idea of using that plant as feedback element of an oscillating system [37]. By doing this, it is possible to generate a signal whose frequency is proportional to the plant stem impedance. The transmitting system used to inject the signal at the top of the plant has been implemented on a previous work [37]. The signal propagates down to the bottom of the plant, where, through an electrode inserted in the plant, its frequency is measured by the present receiving system.

In section 4.3 a brief illustration of the transmitter will be given, while in section 4.2 the components and the electrical characteristics of the present receiving system will be presented.

4.2 Receiving system

The self-autonomous receiving system presented in this work is composed by the following units: an energy harvesting unit, a signal conditioning module, an ultra-low-power microcontroller unit, and a wireless transmission module. A schematic block diagram of the system architecture is shown in figure 4.1.

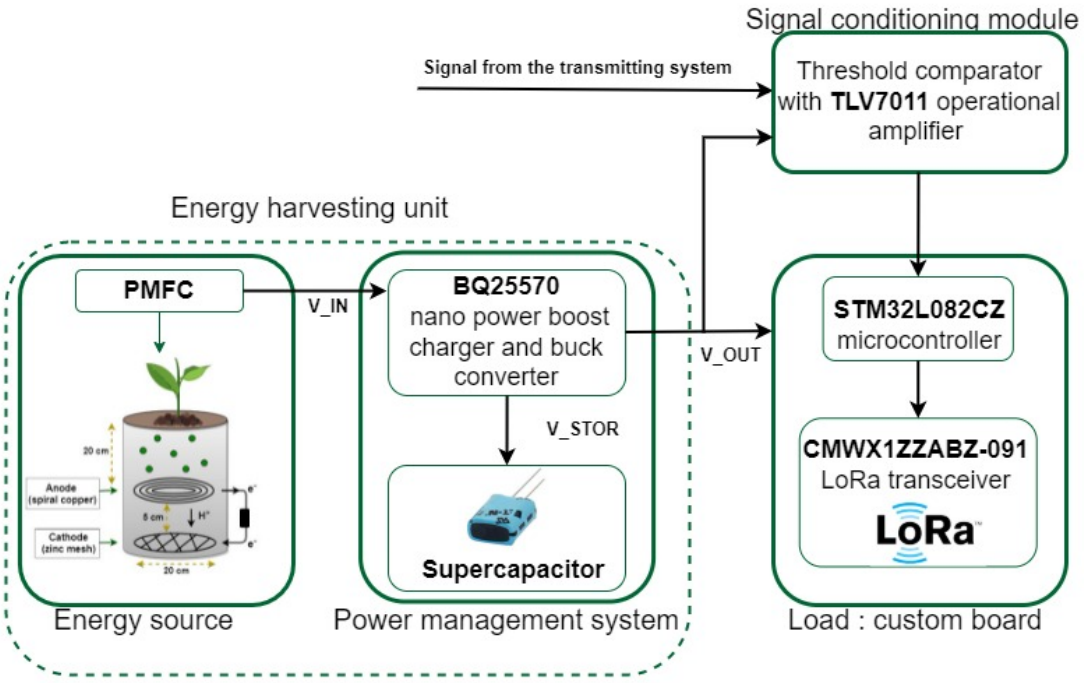

Figure 4.1: Block diagram of the complete receiving system.

4.2.1 Energy harvesting unit

Obtaining a high efficiency in terms of energy extraction and management is of fundamental importance to enable a continuous operation of the sensor node for long periods avoiding the depletion of energy when working with sources of energy that are sporadic and prone to voltage variations due to changes in the environmental conditions. To this end, the use of a power management device and an

energy storage element is required.

Power management system

The BQ25570 nano power boost charger and buck converter for energy harvester-powered applications produced by Texas Instruments has been chosen in this application as *Power Management System* (PMS). The complete module (BQ25570EVM-206 evaluation module) has been used in the implemented system. It is a PCB with the BQ25570 mounted on. In this module, some of the values programmable by the user are fixed by the producer. This is the case of the MPPT and the over voltage value (V_{OV}). The device's characteristics that make it suitable for the current application will be highlighted in the following list.

- *Ultra low power DC/DC boost charger.* As stated in the data sheet [38], the device meets the needs of ultra-low-power applications (as the ultra-low-power sensor node presented in this work), which have stringent power demands. The dc/dc boost converter starts working with very low input voltage ($V_{cold-start} \geq 330$ mV) and, once activated, can harvest energy down to low input voltage (as low as 100 mV). This characteristic is necessary to extract energy from small energy harvesting systems which provide small amounts of output power, like the plant microbial fuel cell presented in this work.

- *Programmable regulated output.* The cell, which is connected to the VIN_DC pin of the power management module (as shown in figure 4.2), provides a voltage high enough to power the BQ25570. The latter provides an externally programmable regulated output (set in this case to $V_{out} = 3.3$V), which is optimized to guarantee high efficiency in a wide range of output currents (from $I_{out} < 10\ \mu$A to $I_{out} \sim 110$ mA). The loading circuit (namely the custom board that embeds the MCU and the transceiver and the signal conditioning module), which the voltages provided by the PMFC could not power, is attached to the VOUT pin of the PMS, which supplies it with this regulated voltage.

- *Maximum power point tracking.* In order to transfer the maximum amount of power from the harvester (which is not an ideal voltage supplier) to the device is necessary to work around the MPP. This is performed by setting the voltage that is sampled and held on the VREF_SAMP pin to the 80% or 50% of the V_{OC}. To set the working point to one of these values, the user must simply pull VOC_SAMP pin high or low, respectively. As already stated, these two values are fixed by the producer since the BQ25570 evaluation module

(EVM) has been employed. If the user wants to set this value to any other fraction, a customized external resistive net must be used. The MPP of the implemented PMFC is not constant, and it changes from $V_{MPP} \simeq 0.45 \cdot V_{OC}$ in the first cell characterization to $V_{MPP} \simeq 0.35 \cdot V_{OC}$ in the third characterization. Considering the two settable values, the V_{MPP} is set to be 50% of the V_{OC} since it is closer to the actual value, avoiding adding external resistors.

- *Energy storage.* The operation of the loading circuit is ensured even when the energy harvester does not provide enough power by using an energy storage element. The BQ25570 supports a variety of energy storage elements: Li-ion batteries, thin-film batteries, supercapacitors, or conventional capacitors. In this application, a 1F supercapacitor has been selected. It is connected to the VSTOR pin of the power management circuit, as shown in figure 4.2. The system provides continuous monitoring of the voltage across the storage element, which is compared to the values of under-voltage (UV) (internally set) and over-voltage (OV) (programmable by the user) voltages to prevent damages to the supercapacitor. The VSTOR pin is configured by the producer in the evaluation module to deliver up to $V_{store} = 4.18$ V to the storage element. As soon as V_{store} decreases under 1.95 V (internally programmed threshold), the output of the PMS is deactivated ($V_{out} = 0$ V)

Energy storage element

The storage element utilized in the energy harvesting unit is a PM-5R0V105-R supercapacitor manufactured by Eaton with a capacitance C = 1 F, shown in figure 4.3. It is a liquid electrolyte supercapacitor with a cylindrical pack, dimensions 8.5 x 16.8 x 21.5 mm, and a weight of 3.5 grams. It uses the *Electrochemical Double Layer Capacitor* (EDLC) construction, which means that the electrostatic storage of energy occurs with the charge separation at the interface between the conductive electrode and the liquid electrolyte.
This series of supercapacitors presents the following features:

- *Low equivalent series resistance (ESR) with high energy density:* the nominal ESR for 1 F supercapacitor measured @ 1 KHz is ESR = 0.15 Ω, while @ 100 Hz ESR = 0.20 Ω.
- *High capacitance*: 0.1 F to 3.0 F.
- *Long cycle life:* with respect to batteries, supercapacitors can stand a significantly higher number of charge/discharge cycles without showing a deterioration of the performances.

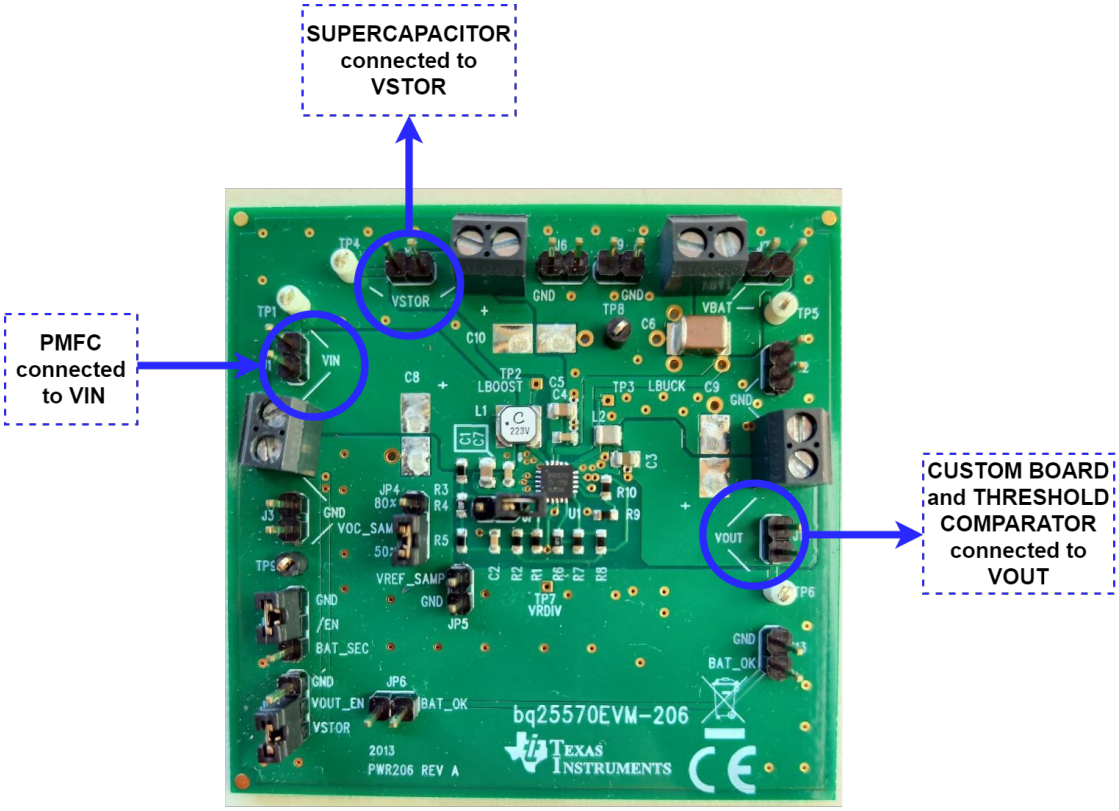

Figure 4.2: Picture of the BQ25570EVM-206 evaluation module.

- *Low leakage currents:* the nominal leakage current for 1 F supercapacitor after 100 hours of usage @ 5.0 V, +20 °C is $I_{leakage} = 10\ \mu A$.

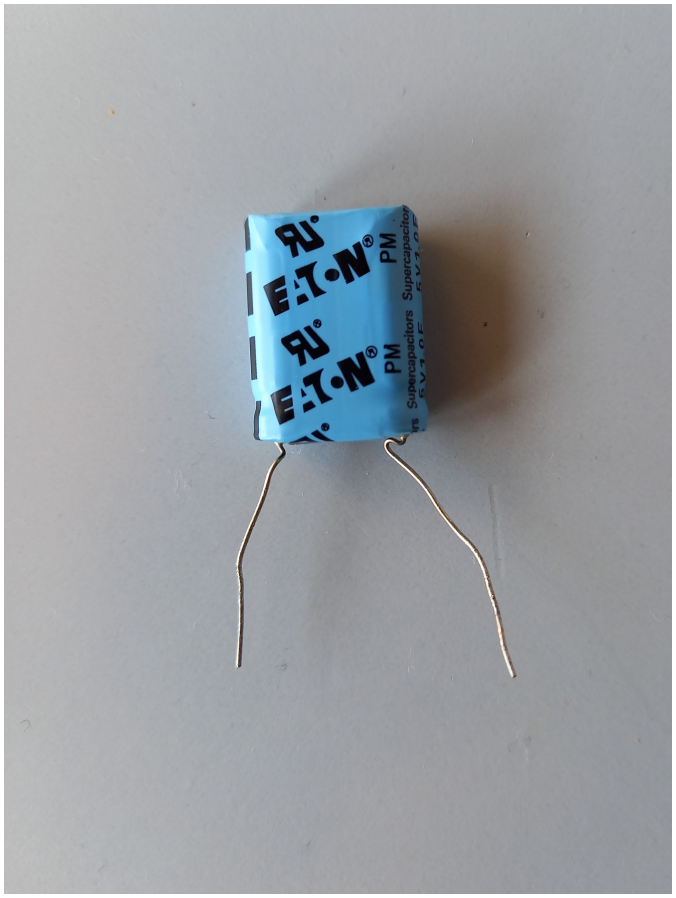

Figure 4.3: Picture of the 1 F supercapacitor

4.2.2 Microcontroller and wireless transmitting unit

In order to achieve the goal of the long-term operation of the sensor node when powered by energy sources that are power limited, it is necessary to lower the energy consumption of the control and transmitting unit. This reduction of the energy requirements can be accomplished with a customized hardware design and intelligent management of power.
For this reason, an ultra-low-power custom board embedding a microcontroller module and a wireless transmission module has been designed to perform the frequency measurements of the signal sent into the plant by the transmitting system and subsequently send the collected data with the radio to a gateway. The designed custom board is shown in figure 4.4.

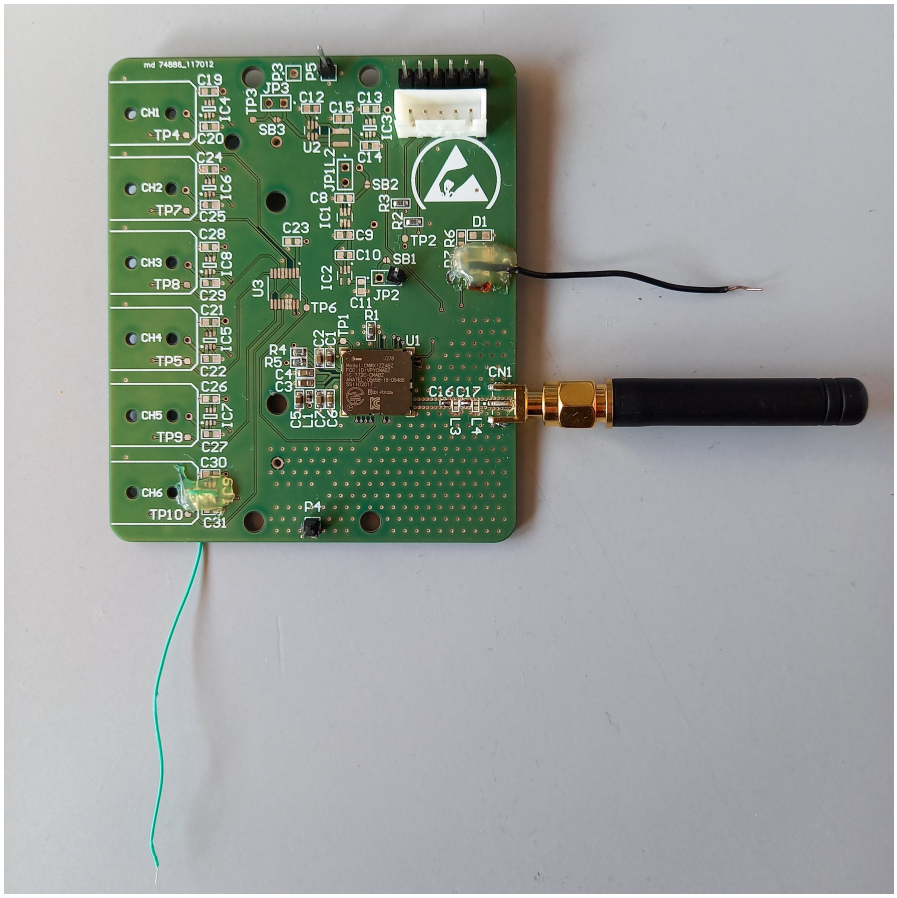

Figure 4.4: Picture of the designed PCB

Ultra-low-power MCU module

The STM32L082CZ is an ultra-low-power microcontroller unit from STMicroelectronics, which can be powered in a voltage range from 1.65 V to 3.6 V. In this application, it is powered by the output voltage of the power management circuit, which is 3.3 V. The core is a 32-bit Arm-based Cortex-M0+ running at up to 32 MHz, with up to 192 KByte of flash memory and 20 Kbyte RAM.
The MCU provides three low-power modes, which present decreasing power consumption and increasing wake-up time so that the best compromise between low power consumption and wake-up time can be achieved depending on the application. Indeed when the MCU runs in *Sleep mode* (first low-power mode), only the CPU is stopped: with this mode, it is possible to reduce the consumption down to 37 μA/MHz, and the wake-up time is only 0.36 μs.
When the *Stop mode* is selected, instead, the lowest power consumption while retaining the RAM content (down to 1.65 μA as stated in the Murata module's

datasheet) can be achieved since the real time clock (RTC) remains active, but all the clocks in the V_{core} domain are stopped. It is possible to wake up the device from the stop mode with any of the EXTI lines (detectors lines constituting the Extended interrupt/event controller) connected to some specific GPIO (General purpose inputs/outputs) pins, but with an increased wake-up time (3.5 μs) with respect to the sleep mode.

Long-Range (LoRa) wireless transmission module

The CMWX1ZZABZ-091 LoRa module from Murata is embedded in the custom printed circuit board (PCB) for the transmission of data from the end-node to the gateway. The module contains the RF Semtech SX1276 low-power transceiver, which features long-range (LoRa) modulation. The LoRa technology is a low-power wide-area network (LPWAN) modulation technique well suited for the IoT since it enables long-range transmissions with low power requirements (since it supports very low bit-rate).
This sub-GHz module operates in the 150 - 960 MHz band depending on the geographical region (868 MHz in Europe). The transceiver, controlled by the STM32L082CZ microcontroller, transmits with a programmable output power in the range of 2 dBm to 18.5 dBm. An omnidirectional antenna is mounted on the edge of the board (right side of the board in figure 4.4) through an SMA connector.

4.2.3 Signal conditioning module

Since the signal received by the system is strongly attenuated after the propagation inside the plant stem, it must be conditioned so that its frequency can be read easily. The use of a signal conditioning module is also needed because the amplitude of the signal generated by the oscillating system is 1.8 V, which is not compatible with the receiving system's electrical characteristics. Indeed, when the STM32L082CZ is powered with 3.3 V voltage supply, the signal must oscillate between 0 V and 3.3 V to be sensed by the microcontroller's external pin.

Threshold comparator

The TLV7011 from Texas Instruments (shown in figure 4.5) has been selected to be the operational amplifier on which an inverting threshold comparator with hysteresis has been built. In order to compensate for the attenuation introduced by the plant, the hysteresis threshold must be chosen to be close. The comparator is powered by the PMS, so it is attached to the VOUT pin of the BQ25570 and receives a 3.3 V supply.

The schematic circuit of the inverting threshold comparator is shown in figure 4.6 where the capacitance C_1 and the resistances R_4 and R_5 composes a high-passing

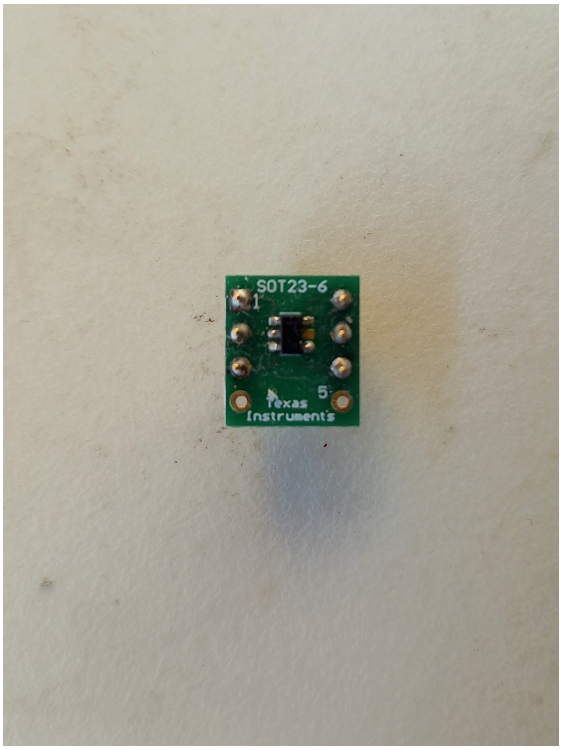

Figure 4.5: Picture of the TLV7011 operational amplifier.

filter. Figure 4.7 shows the bypass capacitances used to decouple the threshold comparator from the power supply. Both the figures are extracted from [37], where the circuit has been implemented.
The details of this threshold comparator will not be given here since the description of all the resistances and capacitances can be found in [37]. The resistances R_1, R_2 ad R_3 determine the threshold levels, and they have been chosen so to have a hysteresis amplitude $\Delta V_{th} = 0.33$ V, given by the difference between the following threshold voltages:

- $V_{th,1} = 1.82$ V
- $V_{th,2} = 1.49$ V

The high-passing filter has been implemented to eliminate the environmental noise and presents a cut-off frequency $f_{cut-off} \simeq 10$ KHz.

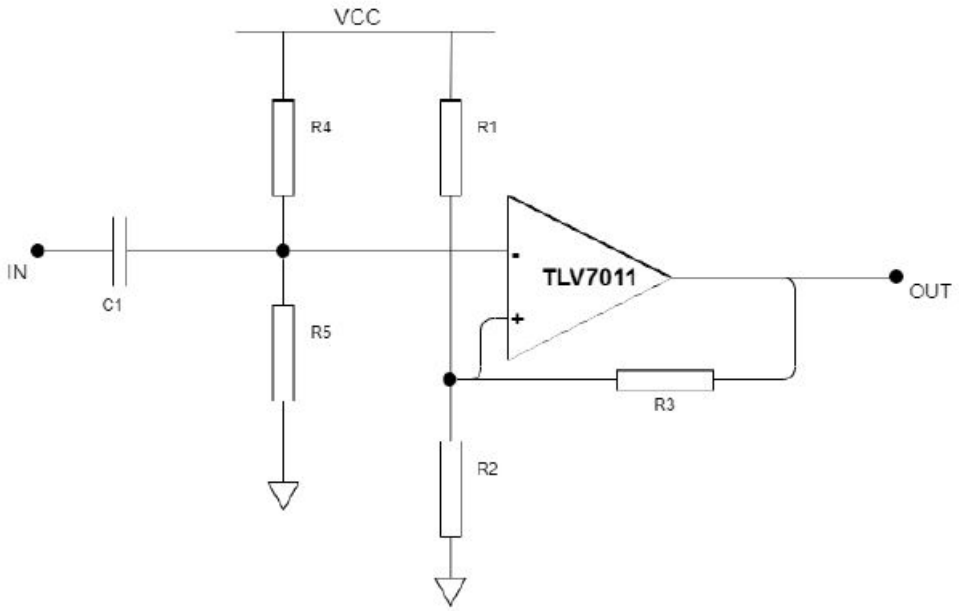

Figure 4.6: Schematic circuit of the threshold comparator.

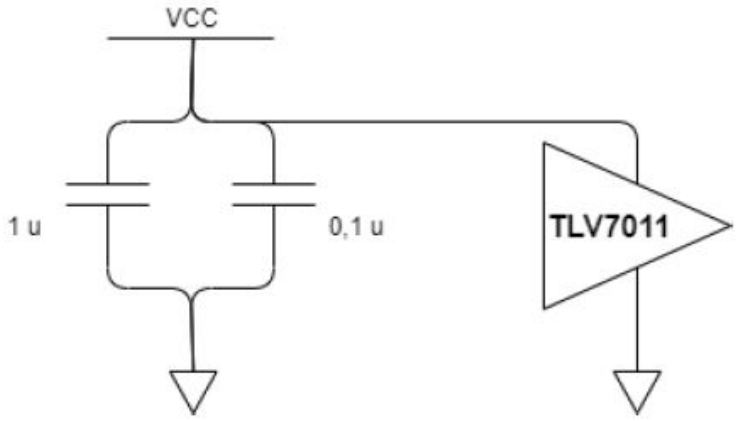

Figure 4.7: Picture of the TLV7011 operational amplifier.

4.3 Transmitting system

The transmitting system is completely autonomous thanks, again, to the harvesting of renewable energy. Indeed two silicon-based solar cells (as the one shown in figure 4.8 extracted from [37]) are used in parallel to power the system since the experiments with one single cell showed that it did not provide enough power.

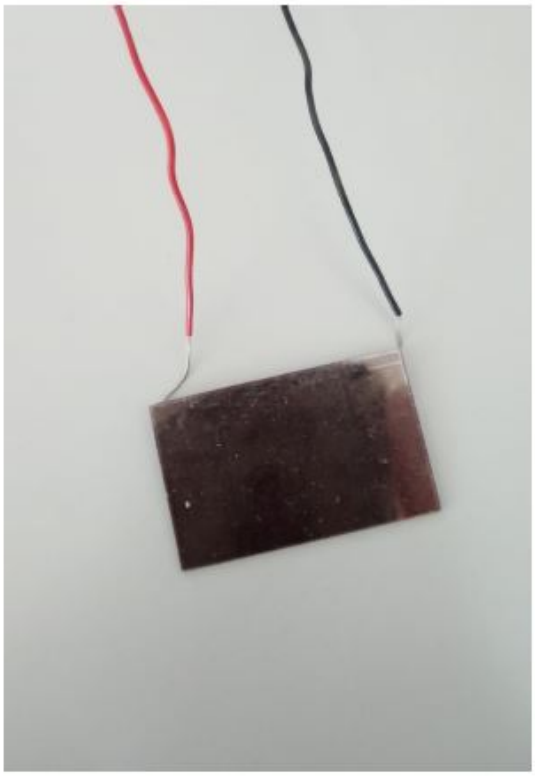

Figure 4.8: Solar cell used to power the transmitting system (two of these cells in parallel).

4.3.1 Power management unit

As for the receiving system, the BQ25570 evaluation module has been chosen as PMS. It is used to extract the optimum amount of power from the solar cells and to manage the accumulation of this energy into the storage element so that the device can operate for an extended lifetime. As a storage element, the same liquid-electrolyte supercapacitor presented in section 4.3 is used.

4.3.2 Timing system

A timing system is used to enable the oscillation into the plant only a few times per hour to save power and ensure a long-lasting operation of the system. This system enables choosing the period between the injection of a signal in the plant

(and the reception of that signal by the receiving system) and the following, which is a prerogative of the power management strategy adopted in the receiving system. Indeed, as will be widely treated in chapter 5, the receiving system's idle state is the stop mode, and it is awakened (with a subsequent peak of consumption) only when a signal from the transmitting system is received or when the collected data are sent to the gateway. With this timing system, it is possible to reduce the consumption by choosing the period with which a signal is sent to the receiving system.
Two timers TPL5110 from Texas Instruments are chosen since they consume a small amount of power, and they can deal with low voltages. They are employed to control the on/off switching of a PMOS which allows the connection from the power management circuit to the rest of the system. In this way, the oscillating system is generally disconnected from the power supply, except for small periodic intervals when a measurement must be performed.
The TPL5110 allows the user to choose the duration of the generated signal through the selection of the external resistance R_{EXT}, according to table 3 of the device data sheet [39].

4.3.3 Oscillator

The LMC555 CMOS timer manufactured by Texas Instruments is the only variation with respect to the transmitting system implemented in [37], where a ring oscillator composed of five inverters was employed. The LMC55 offers low-power dissipation and can run in the following modes depending on the application:

- *Monostable mode*: In this mode, it generates a one-shot pulse, whose width can be set by changing the external capacitance and resistance values.

- *Astable (free-running) mode*: The device acts as an oscillator that generates a continuous rectangular waveform, with duty-cycle and frequency both settable with external resistances and capacitances.

In this application, the LMC555 is used in the astable mode since the output waveform must be generated periodically and not only one time. In particular, the device is configured in the 50% duty-cycle oscillator mode, so the pins are connected as shown in figure 4.9, which is taken from the LMC555 datasheet ([40]) since this configuration is one of the proposed typical applications.

The LMC555 in this configuration generates a square wave with the following frequency:

$$f = \frac{1}{1.4 \cdot R_c \cdot C} \tag{4.1}$$

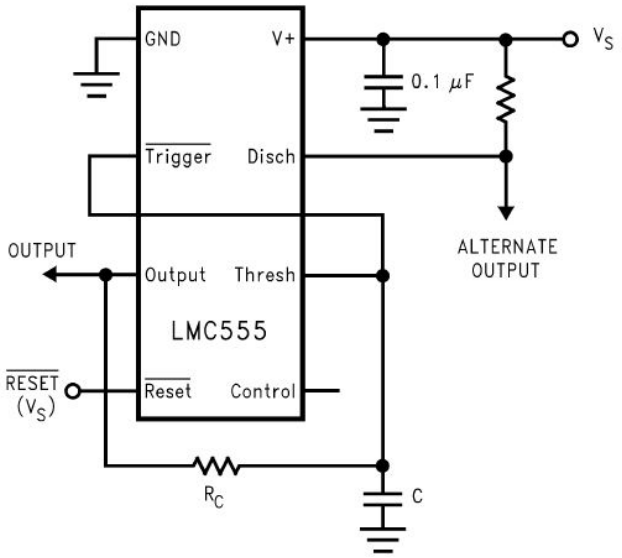

Figure 4.9: LMC555 configured in 50% duty-cycle oscillator mode.

The resistance R_c is constituted by the plant stem electrical impedance. In this way, it is possible to generate a signal with a frequency inversely proportional to the plant impedance, which is, as already stated, the variable under analysis.

4.3.4 Complete transmitting system

The schematic diagram of the complete transmitting system is shown in figure 4.10, which has been extracted from [37] and modified accordingly to the replaced device (LMC555 instead of the ring oscillator to generate the oscillating signal). The signal that comes out from the bottom of the tobacco plant is put as an input of the receiving system and in particular of the signal conditioning module, as shown in figure 4.1.

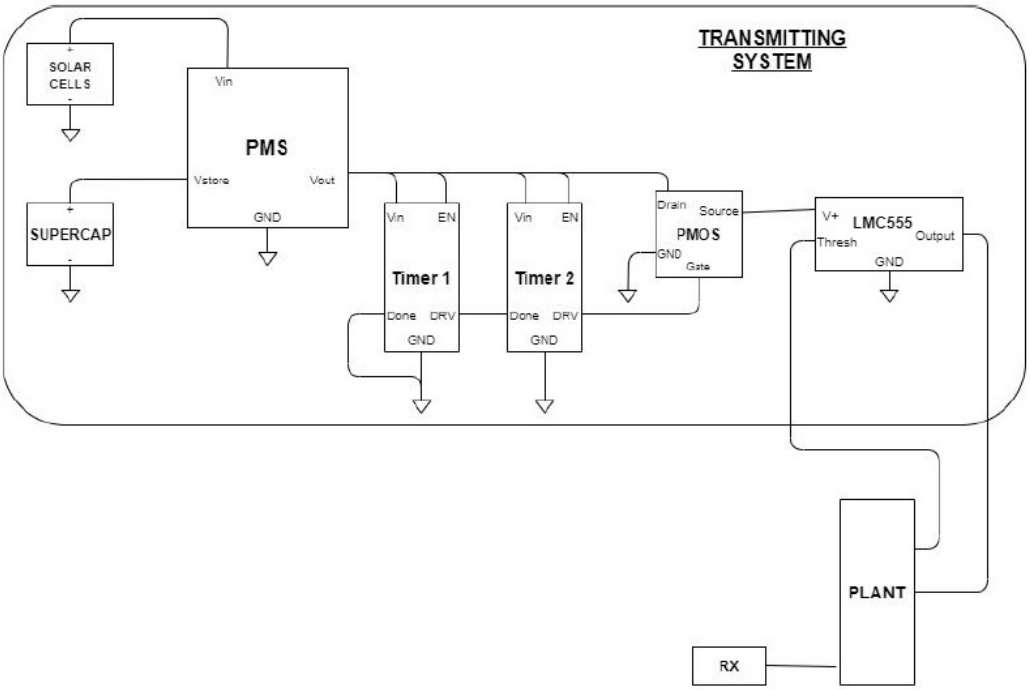

Figure 4.10: Complete transmitting system used to inject a signal into the plant stem. The timers and the PMOS are used to periodically connect the power supplier (solar cells, supercapacitor and PMS) to the load (oscillator).

Chapter 5

Application power management

The Murata module introduced in section 5 is generally provided in a development platform, called STM32 Discovery boards from STMicroelectronics, with which a low-cost development with an STM32 device can be easily started. In this case, the discovery board has not been used since the hardware consumption was too big to be sustained by the PMFC, and a specifically designed custom board has been employed. The custom board, already presented in section 4.4, embeds, as the Discovery boards, an STM32 32-bit microcontroller (in this case the STM32L082CZ) and the CMWX1ZZABZ-091 LoRa module from Murata.
The application code has been built starting from the I-CUBE-LRWAN expansion package, which consists of a set of libraries and application examples for the STM32 microcontrollers based on Arm Cortex -M processor. Before presenting the application, an overview of the LoRaWAN protocol and the LoRa standard will be given in the following section.

5.1 LoRaWAN package overview

The I-CUBE-LRWAN LoRaWAN expansion package is compliant with the LoRaWAN protocol, which is an LPWAN protocol based on the LoRa modulation, which operates in the unlicensed ISM 868 MHz band in Europe. Low power sensors can achieve a long-life operation by reporting over long ranges (up to dozens of kilometers) at a very low bit rate exploiting the LoRa wireless communication network. The integration of LoRaWAN into the IoT is sponsored by the LoRa alliance so that the LoRaWAN ecosystem is in constant growth.
The modulation technique used by the LoRa physical layer (PHY) is the Chirp

Spread Spectrum (CSS) modulation. Long-range transmission of small packets with very low power consumption is achievable with this modulation technique. The end devices can employ the LoRa technology to exchange data among them (end-to-end communication) or to send data to the Internet through gateways. The gateway is a bridge that uses a standard IP connection to the network server and converts the RF packets from the end devices into IP packets and vice versa.

5.1.1 LoRa network

The topology of the LoRa network, shown in picture 5.1 (extracted from [41]), is a star of stars where the gateways collect data from the end-devices in their radius of action and send these packets to a central network server. The end device in this application is an RF transceiver (or radio) and a host STM32 MCU, which implements the radio and the LoRaWAN stack driver.

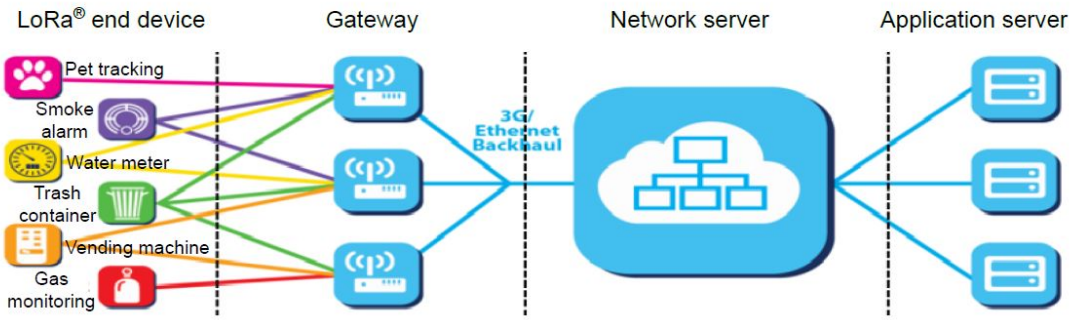

Figure 5.1: LoRa network diagram.

Various classes of end devices are defined by LoRaWAN so that the various IoT applications' needs can be met. The class employed in the present application is the most common, named class-A. When a sensor or actuator has strict energy demands but does not present latency constraints, it exploits the class-A operation, which is the lowest power end-device system. Bi-directional class-A end devices perform an uplink transmission, which is followed by two short downlinks receive windows, as shown in figure 5.2 (taken from [41]). The end device determines the transmission slot depending on its own communication needs.

The end devices must follow a joining procedure to participate and communicate in the LoRa network. In this case, the joining procedure is the OTAA (over-the-air activation): the application server and the end-device have the same secret key

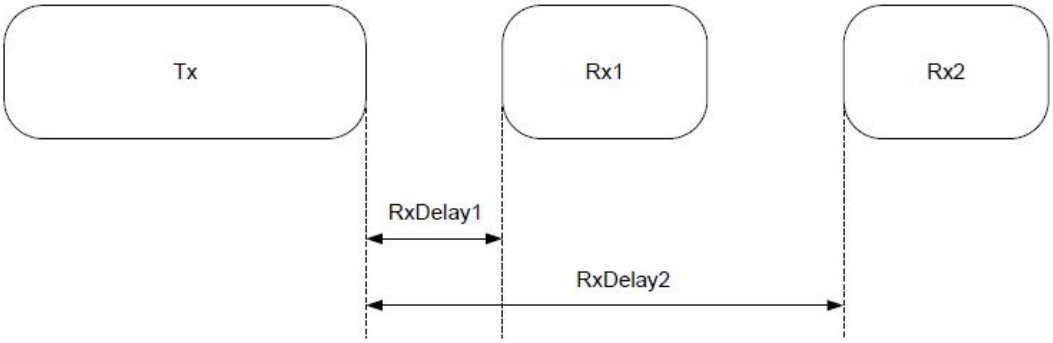

Figure 5.2: Transmission and reception time diagram.

(AppKey), and during the activation, they exchange inputs to generate two session keys:

- A network session key (*NwkSKey*) for the encryption/decryption of MAC (medium access control) commands.
- An application session key (*AppSKey*) for the encryption/decryption of application data.

If, instead, the end device uses the other possible joining procedure called ABP, these two keys are already stored in the end device that sends the data directly to the LoRa network. These two keys ensure the integrity of the MAC payload data (NwkSKey) and the application payload data (AppSKey). Indeed, with the use of the AppSKey, the network server can not interpret the application data sent by the end devices.

5.1.2 Middleware

STM32 microcontrollers can take advantage of the LoRa stack middleware in a source-code format provided with the LoRaWAN expansion package. The latter also includes the STM32L0 HAL (Hardware Abstraction Layer) drivers, which are provided by STMcube together with a set of ready-to-use APIs. The APIs used to control the part of the MCU hardware employed in the application simplify the application implementation. The three important utilities provided by the package are:

- A *sequencer* which offers a service to handle tasks. It provides the possibility to easily execute tasks in the background and enter the low-power modes when no activity is required.

- A *timer* server provides the timer service. It is employed to manage the execution of timed tasks. When a task has to be executed, the system is awakened from the stop mode. The system's wake-up is possible thanks to the RTC (on which the hardware timer is based), which continues to run even in low-power modes.

- A *low-power management* module, which manages the low-power (stop mode) entry when the system goes in the idle state.

An intermediate level of software (*LmHandler.c*) is provided to the user so that an application can be built without worrying about the LoRa state machine. This interface file employs a set of APIs to implement the state machine at the application level. An infinite loop is the application's center, which handles the low-power and runs the interrupt handlers to wake up the system when needed. The sequencer manages all the running tasks.
Figure 5.3 (extracted from [41]) shows the operational model for the LoRaWAN End Node application. After the reset, the system is initialized (HAL, hardware, and LoRa stack), and the LoRa is configured with the specified parameters. As shown in figure 5.4 (taken from [41]), the system goes into an *Init* state. The LoRa end node requests then to join the network (OTAA joining procedure) and enters the *Join* state (figure 5.4). If the joint is correctly performed, the end device can start communicating in the network, thus the LoRa transmission event is initialized (figure 5.3), and the system enters the idle state (*Sleep* in figure 5.4).
The interrupts are enabled so that the process events can be performed. With this application, it is possible to have a radio event (send a packet) either with a timer event or a send event (transition on an external pin). As can be observed from the LoRa state diagram in figure 5.4, after a timer event, the system goes from one of the possible low power modes in a temporary *Joined* state before entering the *Send* state, while with OnSendEvent it enters the *Send* state directly. After the radio event, the system enters the low power mode again, waiting for another transition on the external pin or until when the configured timer period elapses.

In the following section, the application code developed starting from this model will be presented.

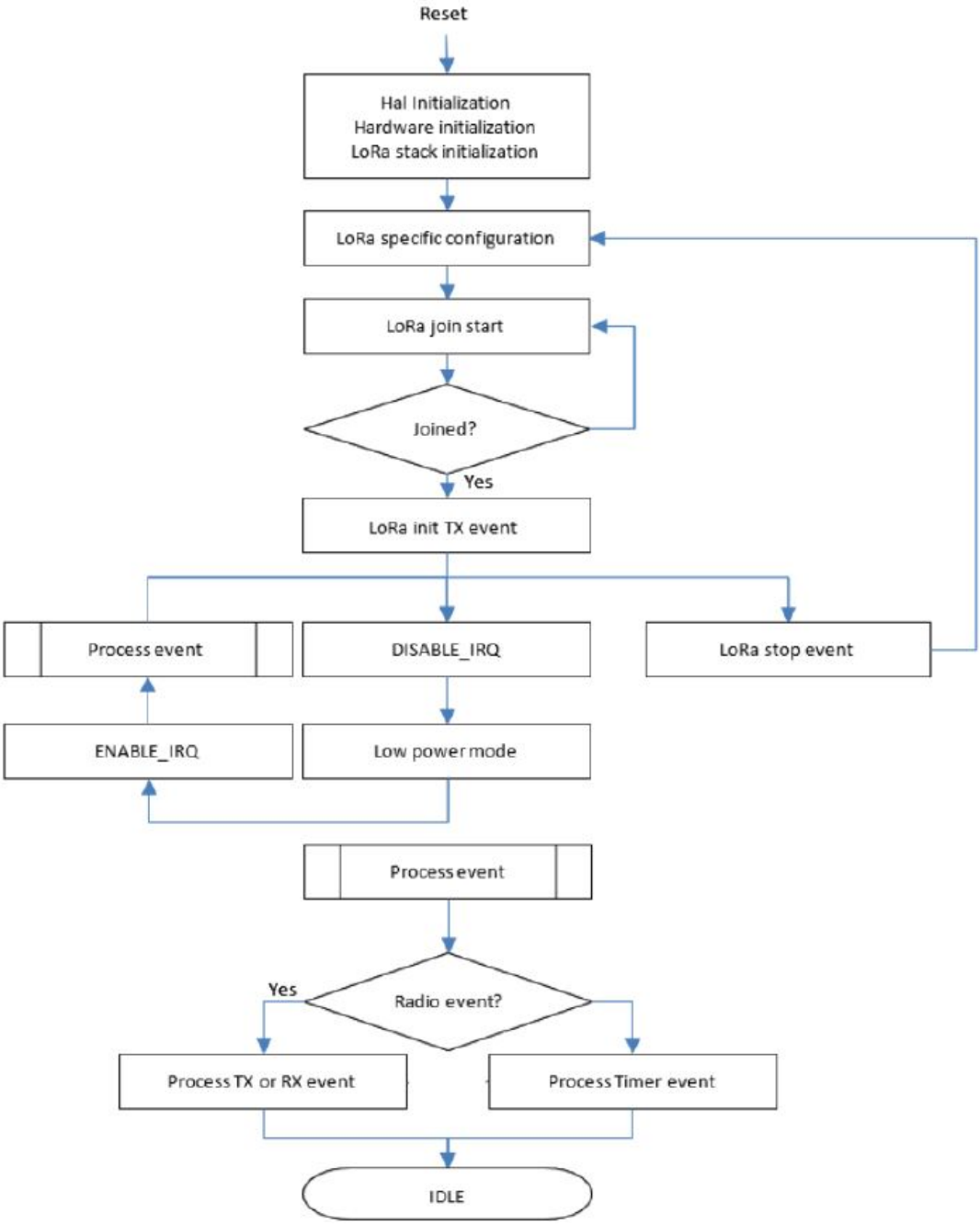

Figure 5.3: LoRaWAN end node operational model

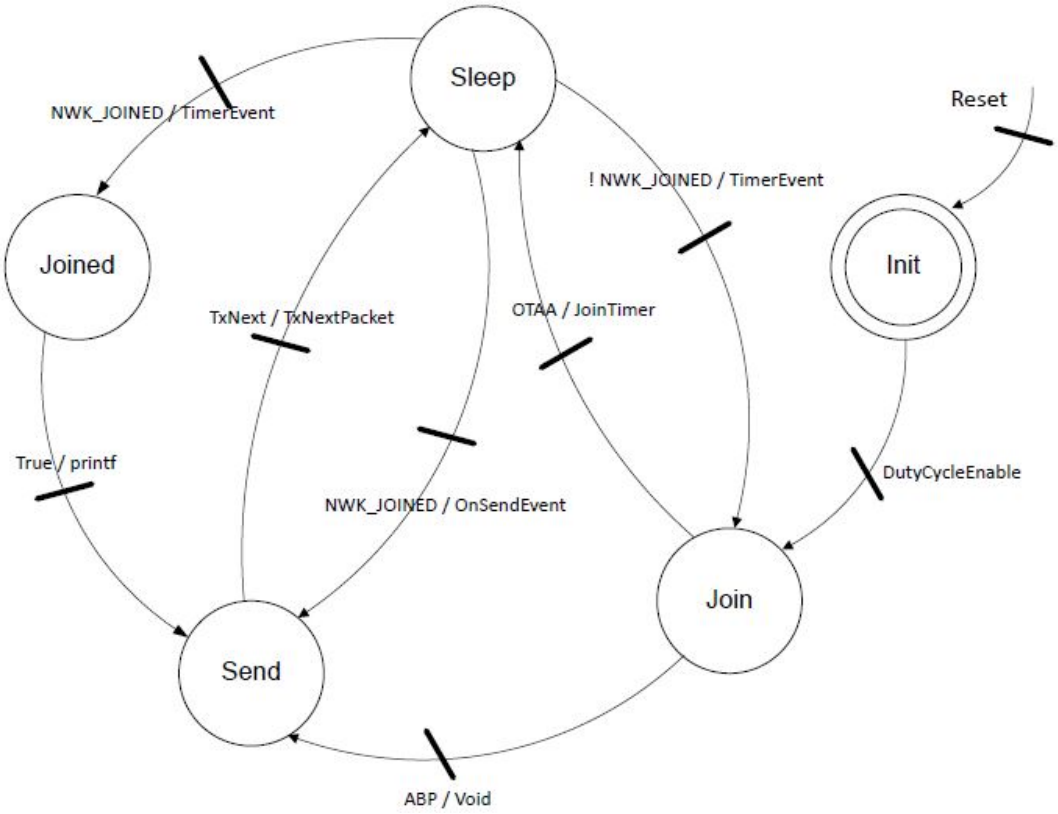

Figure 5.4: LoRa state diagram

5.2 Application code

5.2.1 Initialization functions

The first part of the main function shown in listing 5.1 is where the initialization functions are placed.

Listing 5.1: Initialization code

```
1
2
3 int main(void)
4 {
5   /* MCU Configuration
      --------------------------------------------------------*/
6
7   /* Reset of all peripherals, Initializes the Flash interface and
      the Systick. */
8   HAL_Init();
9
```

```
10   /* Configure the system clock */
11   SystemClock_Config();
12
13   /* Initialize all configured peripherals */
14   MX_LoRaWAN_Init();
15
16   /* USER CODE BEGIN 2 */
17   MX_TIM2_Init(); /* Initialize timer2 */
18   MX_TIM3_Init(); /* Initialize timer3 */
19   MX_GPIOB_Init(); /*Initialize GPIOB */
20   UTIL_SEQ_RegTask((1 << CFG_SEQ_Task_WaitStopMode), UTIL_SEQ_RFU,
       wait); /* Register wait task */
21   /* USER CODE END 2 */
22
23 ...
24 }
```

At line 8 the STM32 HAL libraries are initialized so that all the used peripheral of the microcontroller employed in the application are initialized instead of using a low-level configuration. At line 11 the system clock is configured, and at line 14 the LoRaWAN process is initialized. As explained in section 5.1.2, the user can select the event that triggers the data transmission between an external event (TX_ON_EVENT) or the elapsed time of the timer (TX_ON_TIMER). If the user selects the transmission on timer event (as in the present application), the function that initializes the LoRaWAN process (shown in part in listing 5.2) located in file *lora_app.c* creates a timer (line 9) managed by the timer server utility, sets the period of this timer (line 10) to the value defined by the user (APP_TX_DUTYCYCLE) and starts the timer (line 11).

Listing 5.2: Transmission on timer event

```
1
2  void LoRaWAN_Init(void)
3  {
4  ...
5
6    if (EventType == TX_ON_TIMER)      /* User can choose between
       TX_ON_TIMER and TX_ON_EVENT */
7    {
8      /* send every time timer elapses */
9      UTIL_TIMER_Create(&TxTimer,  0xFFFFFFFFU, UTIL_TIMER_ONESHOT,
       OnTxTimerEvent, NULL);
10     UTIL_TIMER_SetPeriod(&TxTimer,  APP_TX_DUTYCYCLE);
11     UTIL_TIMER_Start(&TxTimer);
12   }
13
14   ...
```

```
15 }
```

Line 20 of listing 5.1 registers a task in the sequencer to avoid the system entering the stop mode while the timer interrupts must be served and will be better explained in section 5.2.3. Line 17, 18 and 19 of the same listing initialize the timers (TIM2 and TIM3) and the GPIOB and, differently from the previous initializations, these peripherals are specifically initialized for this application.
TIM2 and TIM3 peripherals are 16-bit general-purpose timers counting up and down, with a programmable prescaler used to divide the clock frequency by a 16 bit factor to scale it down. TIM2 is configured in **input capture** mode since it is used to perform the frequency measurement. Channel 1 of the timer is connected to the external general-purpose I/O pin PA5 so that every time a rising edge is detected on that pin, an interrupt is fired (if this function is enabled by the user). The value of the counter after a detected transition is saved in the Capture/Compare registers (TIMx_CCRx).
TIM3 is configured in **output compare** mode since it is used to indicate when a certain period of time has elapsed. If the interrupt generation is enabled, an interrupt is fired every time a match is found between the capture/compare register TIMx_CCRx (where the period to be measured must be loaded) and the counter. Since the timer includes four independent channels, two different channels are configured both in output compare mode. Channel 1 is configured to generate an interrupt after 3 s, while Channel 2 is configured to generate an interrupt after 500 μs. The utility of measuring these two periods will be explained in section 5.2.3.
The GPIOB peripheral initialization is done to configure PB2 as EXTI with interrupt generation. It is configured such that when a rising edge on that pin is detected, the system is awakened from the stop mode through the EXTI controller's line corresponding to the pin. The EXTI controller is a service peripheral used by other peripherals to manage the asynchronous events and send an event request to the CPU and a wake-up request to the power controller.
In all these three initialization functions, the specific peripheral interrupts are enabled in the NVIC interrupt controller with the function provided by the HAL libraries.

5.2.2 Loop function

The center of the application is the infinite loop shown in listing 5.3. Line 6 calls the sequencer, which manages the execution of all the pending tasks. When all the interrupts have been served, and there are no more tasks to be executed, the machine enters the stop mode.

Listing 5.3: Loop function

```
1
2   while (1)
3   {
4     /* USER CODE END WHILE */
5
6      MX_LoRaWAN_Process();
7
8     /* USER CODE BEGIN 3 */
9
10   /* USER CODE END 3 */
11  }
12 }
```

5.2.3 Interrupt callbacks

The management of the power in the application is based on waking up the system from the idle state *Sleep* shown in figure 5.4 only in the two following cases:

- When a frequency measurement has to be performed. This happens when a rising edge is detected on pin PB2, where the oscillating signal from the transmitting system (after being conditioned by the threshold comparator) is sent. The timing of the measurements is managed by the timing system of the transmitting system: every time a signal is sent into the plant, the receiving system is awakened by the interrupt on the EXTI line.
- When a LoRa packet has to be sent since the transmission timer has elapsed. The transmission duty cycle is set by the user through the parameter *APP_TX_DUTYCYCLE*.

The application's power management strategy is shown in figure 5.5. The system wake-up time from the stop mode to the run mode is 3.5 μs.

The oscillating signal is also sent on the external pin PA5, connected to Channel 1 of TIM2. Indeed, the frequency evaluation is based on the measurement, through the input capture function, of the difference in the counter between two consecutive signal's rising edges, which corresponds to the signal's period.

PB2 EXTI line interrupt callback

The system is awakened from the stop mode when a rising edge on PB2 is detected. When the interrupt mode is selected, the ISR calls the callback function, which must be implemented by the user. The callback function for the PB2 EXTI line interrupt is shown in listing 5.4.

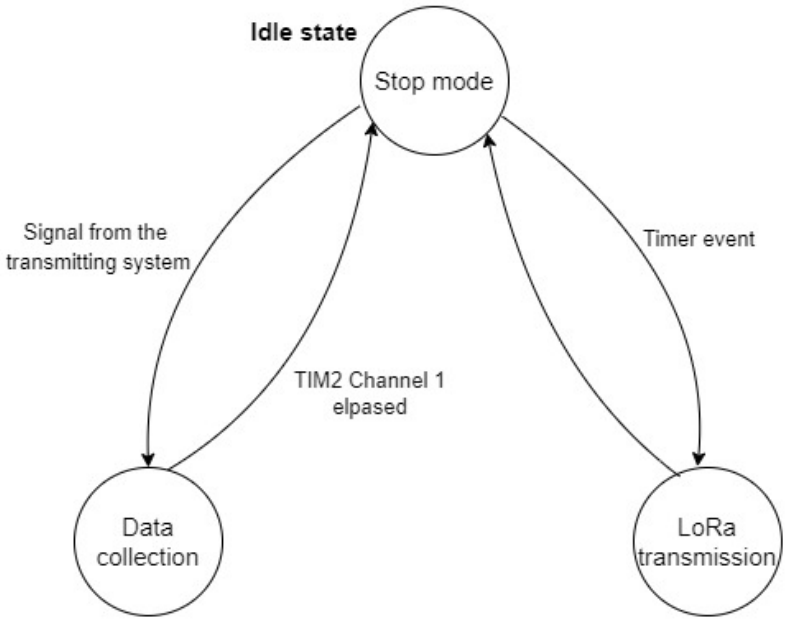

Figure 5.5: Application state diagram.

First, at line 5, the interrupt generation for the EXTI line connected to the GPIO PB2 is disabled to avoid the following signal's rising edges calling this function again. The interrupt generation will be enabled again after the frequency has been evaluated. Lines 7-9 start the configured timers in interrupt mode through the high-level functions provided by the ST HAL.
The rest of the application is based on serving the interrupts from the timers, which are not running in stop mode. Indeed, as already explained, only the RTC continues to run in this low-power mode. Since the system would return to sleep after serving the PB2 interrupt, the CFG_SEQ_Task_WaitStopMode task is set in line 13. With flag set to 1 in the interrupt callback, the *wait* function shown in listing 5.7 associated with the task enters a while loop, used to keep the machine in run mode so that it is sensitive to the timers interrupts.

Listing 5.4: PB2 EXTI line interrupt callback

```
1
2 void HAL_GPIO_EXTI_Callback(uint16_t GPIO_Pin) {
3
4     if(GPIO_Pin == GPIO_PIN_2){ /* A rising edge is detected on PB2
    */
5         HAL_NVIC_DisableIRQ(EXTI2_3_IRQn); /* Disable EXTI line
    interrupt connected to PB2 at NVIC level */
```

```
6           TIM3 -> CNT = 0; /* Reinitialize counter register of TIM3 to
    0 */
7           HAL_TIM_OC_Start_IT(&htim3, TIM_CHANNEL_1); /* Start Channel
    1 of TIM3 in output compare mode, with interrupt generation
    enabled */
8           HAL_TIM_OC_Start_IT(&htim3, TIM_CHANNEL_2); /* Start Channel
    2 of TIM3 in output compare mode, with interrupt generation
    enabled */
9           HAL_TIM_IC_Start_IT(&htim2, TIM_CHANNEL_1); /* Start Channel
    1 of TIM2 in input capture mode, with interrupt generation enabled
     */
10          HAL_NVIC_EnableIRQ(TIM2_IRQn); /* Enable TIM2 interrupt at
    NVIC level */
11          HAL_NVIC_EnableIRQ(TIM3_IRQn); /* Enable TIM3 interrupt at
    NVIC level */
12          flag = 0;
13          UTIL_SEQ_SetTask((1 << CFG_SEQ_Task_WaitStopMode),
    CFG_SEQ_Prio_0); /* Request to the sequencer to execute the
    function wait(), with flag
14          set to 0 */
15      }
16  }
```

TIM2 input capture callback

Every time a rising edge is detected on PA5 (connected to TIM2 Channel 1), an input capture interrupt is fired, and the callback shown in listing 5.5 is called. The variable *count* in line 5 is incremented every time an interrupt is received, and its functionality will be explained below.
The following lines are related to the evaluation of the signal's period. When the first rising edge is detected, the value of the counter is saved in the variable *capture*. When the second rising edge is detected, the application enters the input capture callback again. The value of *capture* is saved in another variable (*capture_old*) and the new content of the capture/compare register is saved in *capture*. This mechanism is repeated for each input signal's rising edge. After the capture has been performed, the flag *captureDone* is set to 1 so that the frequency can be evaluated in the *wait* function, shown in listing 5.7.

Listing 5.5: TIM2 input capture interrupt callback

```
1
2  void HAL_TIM_IC_CaptureCallback(TIM_HandleTypeDef *htim)
3    {
4
5      count++; /* Increase the variable each time a rising edge is
    detected */
```

```
6       if (htim->Channel == HAL_TIM_ACTIVE_CHANNEL_1)
7       {
8           capture_old = capture;
9           capture = TIM2->CCR1; /* Save the capture/compare register
        content */
10          captureDone = 1;
11
12      }
13  }
```

TIM3 elapsed time callback

Listing 5.6 shows the callback function that is called when the TIM3 interrupts are fired. TIM3 Channel 2 is used to indicate when a period of 500 μs (starting from the rising edge on PB2 that awake the system) elapsed. At the end of this interval (line 8), the number of detected edges (variable *count* in line 10) is checked. If the number of edges detected in 500 μs is smaller than three, it means that the commutations on PA5 were not due to the signal from the transmitting system but only to a spike due to the environmental noise. Thus the timers are stopped, and the system returns in stop mode (since *flag* is set to 1 at line 18) without continuing with the frequency evaluation. This software-level filter was added to the hardware high-passing filter introduced in subsection 4.2.3 since, during the real simulations, the glitches registered on the pin were very frequent. In this way, in case of a spike, the system is awakened for a very short period (500 μs), reducing the power consumption and enhancing the lifetime.
If the commutations on PA5 were more than three, they were actually due to the oscillating signal. In this case, the system continues to run until an interrupt is fired by the elapsed time of TIM3 Channel 1. This channel indicates when 3 s have passed since the first rising edge is detected on PB2, which correspond to the frequency measurement interval. In the interrupt callback (line 31), the variable *write* is set to 1 so that after the 3 s, only the last computed frequency value is written in a circular array. The LoRa payload will be constituted by the average of the array's values. This will be better explained in section 5.2.4.

Listing 5.6: TIM3 delay elapsed callback

```
1
2
3  void HAL_TIM_OC_DelayElapsedCallback(TIM_HandleTypeDef *htim)
4  {
5
6      if(check == 0){
7
```

```
8         if(htim->Channel == HAL_TIM_ACTIVE_CHANNEL_2){ /* TIM3
    Channel 2 period elapsed */
9
10            if (count <= 3){ /* In 500 us the edges detected are less
     than 3 */
11                HAL_TIM_OC_Stop_IT(&htim3, TIM_CHANNEL_1); /*
    Stop TIM3 Channel 1 */
12                HAL_TIM_OC_Stop_IT(&htim3, TIM_CHANNEL_2); /*
    Stop TIM3 Channel 2 */
13                HAL_TIM_IC_Stop_IT(&htim2, TIM_CHANNEL_1); /*
    Stop TIM2 Channel 1 */
14                TIM3 -> CNT = 0; /* Reinitialize TIM3 counter to
    0 */
15                HAL_NVIC_DisableIRQ(TIM2_IRQn); /* Disable TIM2
    interrupt at NVIC level */
16                HAL_NVIC_DisableIRQ(TIM3_IRQn); /* Disable TIM3
    interrupt at NVIC level */
17                count = 0; /* Reinitialize the number of detected
     rising edges to 0 */
18                flag = 1; /* Exit the wait function and enter the
     stop mode */
19                __HAL_GPIO_EXTI_CLEAR_IT(GPIO_PIN_2); /* Clear
    PB2 pending interrupts */
20            }
21            else {
22                count = 0; /* Reinitialize the number of detected
     rising edges to 0 */
23                check = 1; /* Avoid entering this if statement
    again */
24            }
25        }
26    }
27
28    else{
29        if(htim->Channel == HAL_TIM_ACTIVE_CHANNEL_1) /* TIM3 Channel
     1 period elapsed */
30        {
31            write = 1; /* Set the flag to 1 to write the frequency
    value in the array */
32            HAL_TIM_OC_Stop_IT(&htim3, TIM_CHANNEL_1); /* Stop TIM3
    Channel 1 */
33            HAL_TIM_OC_Stop_IT(&htim3, TIM_CHANNEL_2); /* Stop TIM3
    Channel 2 */
34            HAL_TIM_IC_Stop_IT(&htim2, TIM_CHANNEL_1); /* Stop TIM2
    Channel 1 */
35            TIM3 -> CNT = 0; /* Reinitialize TIM3 counter to 0 */
36            HAL_NVIC_DisableIRQ(TIM2_IRQn); /* Disable TIM2 interrupt
     at NVIC level */
```

```
37              HAL_NVIC_DisableIRQ(TIM3_IRQn); /* Disable TIM3 interrupt
    at NVIC level */
38              count = 0; /* Reinitialize the number of detected rising
    edges to 0 */
39              check = 0; /* Enable the check if statement */
40              __HAL_GPIO_EXTI_CLEAR_IT(GPIO_PIN_2); /* Clear PB2
    pending interrupts */
41
42          }
43      }
44  }
```

5.2.4 Frequency evaluation

The frequency evaluation is performed in the *wait* function shown in 5.7. When a rising edge has been detected, flag *captureDone* is set to 1 in the TIM2 interrupt callback so that the if statement at line 5 is entered. First, the case in which TIM2 reached the overflow after the first rising edge (line 7) is analyzed to correct the captured values. Then, frequency is evaluated (line 12) by simply dividing the frequency at which the timer is running by the difference between the two captured values (signal's period).
As already stated, when the configured measurement period has elapsed, flag *write* from the TIM3 interrupt callback is set to 1 so that the if statement at line 17 is entered. The square wave generated by the oscillating system in the transmitter could be not so stable, having a slightly changing frequency during the signal's duration. The strategy adopted to address this issue is to repeat the frequency evaluation with all the signal periods. At the end of the measurement period, only the average of all the computed values is taken and written in a circular array (line 23). Since the variable *flag* is set to 1 in line 27, after the last if statement is served, the application exits the while loop, and the machine returns in stop mode.
The LoRa payload that is sent (managed in the *lora_app.c* file) is the average of the frequencies values that have been written in the array since the last transmission. If a transmission has been performed, the application enters the if statement at line 29. Here, the array is reinitialized to 0 and the frequency to its default value (-1) so that if no measurements have been performed since the last transmitted packet, the payload is -1. Before exiting the *wait* function, the PB2 EXTI line interrupt generation is enabled again (line 44) so that the following signal from the transmitter can awake the system.

Listing 5.7: Wait function

```
1
```

```
2  void wait(void){ /* Wait function associated with the
       CFG_SEQ_Task_WaitStopMode task, used to avoid the machine entering
        the stop mode */
3
4      while(flag == 0){
5
6          if (captureDone == 1) { /* Two consecutives rising edges have
        been detected on PA5 */
7                  if(capture < capture_old)
8                      diffCapture = capture - capture_old + 65535;
9                  else
10                     diffCapture = capture - capture_old;
11
12             frequency = HAL_RCC_GetPCLK1Freq() / (htim2.Instance->
       PSC + 1) / diffCapture; /* Evaluate the frequency */
13             captureDone = 0; /* Reset variable */
14             sum += frequency; /* Sum all the computed frequencies */
15             a++; /*Increment a every time a frequency is computed */
16             }
17
18             if(write == 1){
19                 average = sum/a; /* Compute the average */
20                 averageFreq = (uint16_t)average; /* Cast to 16 bit
       int */
21                 sum = 0; /* Reset variable */
22                 average = 0; /* Reset variable */
23                 a = 0; /* Reset variable */
24                 arrayFreq[b++%5] = averageFreq; /* Write the value of
        frequency in a circular array. b keep the positions of the array
       that have
25
26                    been written*/
26                 write = 0; /* Reset the flag */
27                 flag = 1; /* Exit the wait function and enter the
       stop mode */
28             }
29
30             if(sent == 1){ /* The packet has been sent */
31
32                 for(i=0; i<5; i++){
33                 arrayFreq[i] = 0; /* Reset the array */
34                 }
35
36                 b = 0; /*Reset the variable */
37                 freq = -1; /* Default value of frequency */
38                 sent = 0; /* Reset the flag */
39
40
41             }
```

```
42
43      }
44      HAL_NVIC_EnableIRQ(EXTI2_3_IRQn); /* Re-enable EXTI line
        interrupt connected to PB2 at NVIC level */
45  }
```

Chapter 6

Experimental results

The system has been assembled with the components mounted on a breadboard as shown in figure 6.1 to perform real tests. The transmitting system (circled in black in the picture) is powered by the solar cells and uses a tobacco plant as feedback element of the oscillating system. A square wave is injected into the plant stem through the needles connected with the green crocodile clips (figure 6.2). The PMFC-powered receiving system receives the oscillating system that is extracted at the bottom with the red cable (figure 6.2) connected to the lowest electrode. The performance of the autonomous sensor node system and the data analysis will be discussed in this chapter.

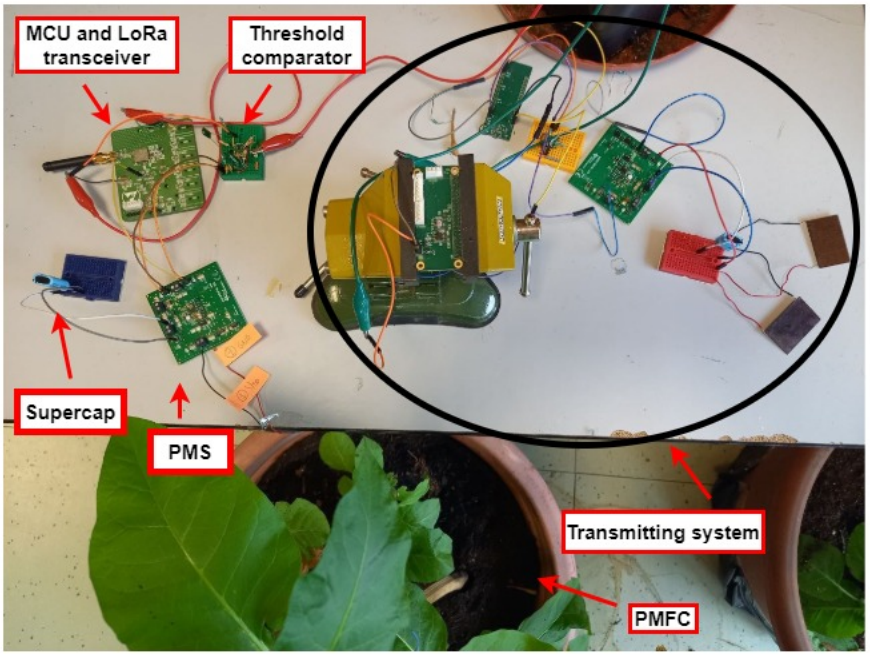

Figure 6.1: Picture of the implemented sensor node.

Figure 6.2: Picture of the tobacco plant used as oscillating system's feedback element.

6.1 Receiving system power budget

The receiving system power consumption has been evaluated considering the power management strategy introduced in section 5.2.3. Due to the environmental noise, the connection of the transmitting system causes spurious transitions on the wake-up pin. In order to avoid this issue, in this first part of the tests, the oscillating signal to be analyzed is produced by the 33220A waveform generator from Agilent Technologies. The instrument is controlled remotely with a LabVIEW script configured to generate a square wave periodically, with a duration of 1 second, an amplitude of 3.3 V, and an offset of 1.65 V. The frequency of the signal changes with a known simple algorithm in the range from 10 kHz to 60 kHz. The period with which the system receives the signal and wakes up to perform the frequency measurement is $T_{meas} = 10$ min. The transmission duty cycle is set to $T_{TX} = 45$ min through the parameter *APP_TX_DUTYCYCLE* so that the LoRa payload will be constituted by the 4/5 frequency values evaluated in between two radio events.
Through the data collection with The Things Network (TTN) (which will be presented in section 6.3), the correctness of the developed code has been demonstrated. Indeed the frequency values constituting the LoRa payloads were in accord with the averages of the values generated by the algorithm.
34401A digital multimeter from Agilent Technologies has been employed to have real measurements of the system's current consumption. Even in this case, the instrument is controlled with a LabVIEW script, which is configured to sample the current value every 200 ms.

The system current consumption sequence in a 200 min interval is illustrated in figure 6.3. When the machine is in stop mode, the mean current consumption is only $I_{stop} \simeq 1.45$ μA, which is not appreciable in the figure. Every ten minutes, the system performs a frequency measurement, where it requires an average of $I_{meas} \simeq 10.5$ mA. In the figure, the data collection states correspond to the lower peaks, marked with black vertical lines. The most current consuming state is instead the LoRa transmission, marked with a red vertical line in figure 6.3. Indeed, the system has an average current consumption of $I_{TX} \simeq 35$ mA when transmitting a payload to the gateway. The consumption peaks are better shown in figure 6.4, where a shorter interval of the previous graph is reported. It illustrates a 51 minutes interval of system monitoring, with two LoRa transmissions and 5 frequency measurements in between.

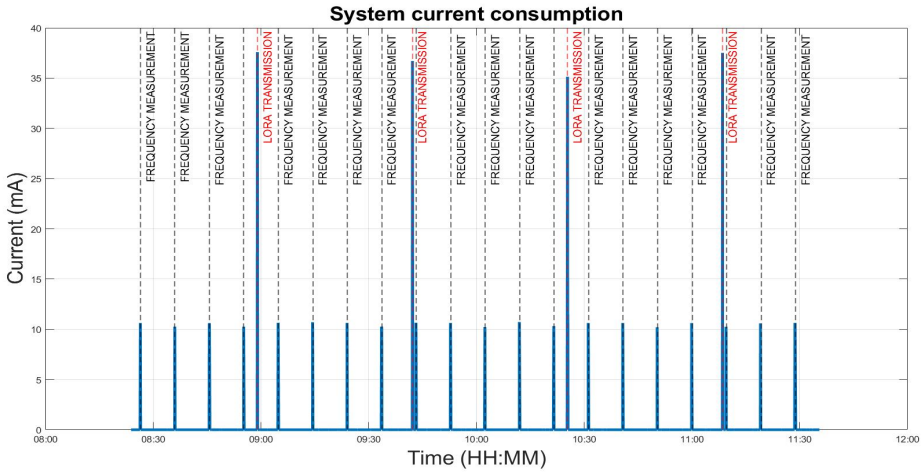

Figure 6.3: Current consumption sequence in a 200 min interval (59870 samples): the frequency measurement states are marked in black, while the LoRa transmission states are marked in red. The rest of the time the system is in stop mode. On the x-axis H = hours, M = minutes.

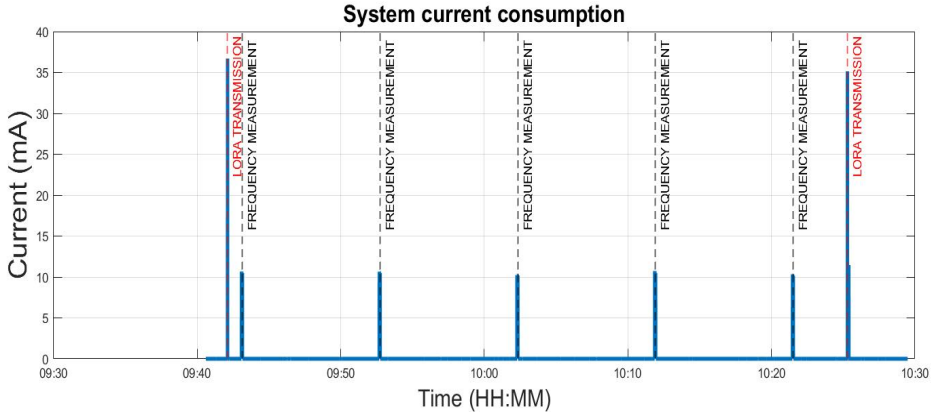

Figure 6.4: Current consumption sequence in a 51 min interval (15270 samples): the frequency measurement states are marked in black, while the LoRa transmission states are marked in red. The rest of the time the system is in stop mode. On the x-axis H = hours, M = minutes.

The current consumption during the interval in which the system wakes up to perform the square wave frequency measurement is shown in figure 6.5, where the duration of the consumption peaks can be appreciated. It can be observed that the system wakes up for 3 s and then enters the stop mode again.

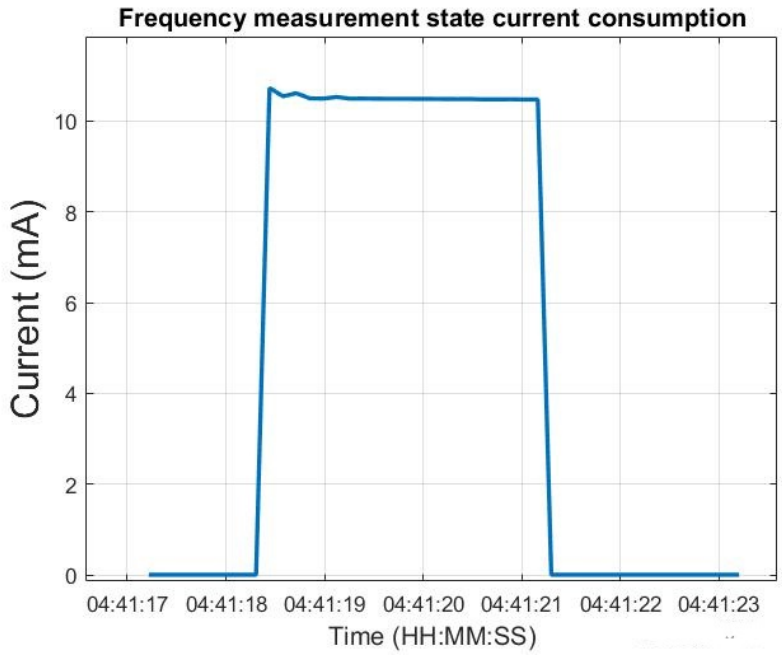

Figure 6.5: System current consumption in the frequency measurement interval. On the x-axis H = hours, M = minutes, S = seconds.

In figure 6.6, the LoRa transmission current consumption is shown. The bi-directional class-A end devices' communication mechanism with the server explained in section 5.1.1 can be clearly observed. Indeed, the current consumption is actually constituted by three peaks that were not distinguishable in figures 6.3 and 6.4 because of the scale on the x-axis. The higher transmission peak corresponds to the LoRa payload transmission from the end device to the gateway, while two smaller consumption peaks correspond to the windows for the downlink communication from the server to the node.
The duration of the slots in which the system is awakened to perform the payload transmission and the confirmation reception can not be deduced from the graph since only one current value is sampled during these slots. However, from the number of sampled values, it is possible to understand that the transmission slot lasts slightly less than the sampling period (200 ms) since during the whole current monitoring, the transmission peak is measured almost every time a packet is sent. The reception windows, shorter than the transmission ones, are instead sampled only a few times.

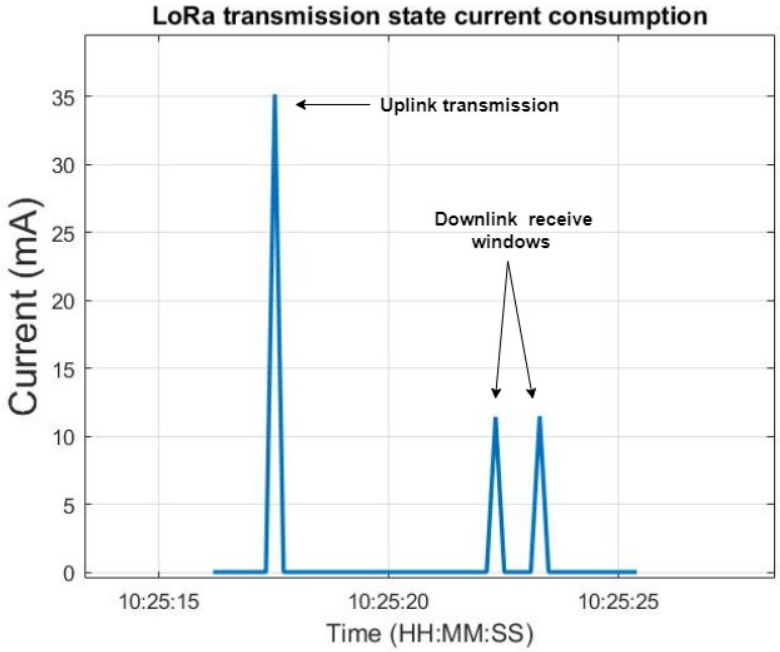

Figure 6.6: System current consumption during LoRa transmission. On the x-axis H = hours, M = minutes, S = seconds.

Figure 6.7 illustrates the system's power consumption sequence in a 1 hour interval, evaluated simply as:

$$P = V_{DD} \cdot I \tag{6.1}$$

where I is the current consumption and V_{DD} the supply voltage (3.3 V). The consumption peaks correspond to an average of $P_{meas} \simeq 34.5$ mW in the frequency measurement state and $P_{TX} \simeq 116$ mW in the transmission state. In stop mode, the system power requirement is on average $P_{stop} \simeq 4.8$ μW.

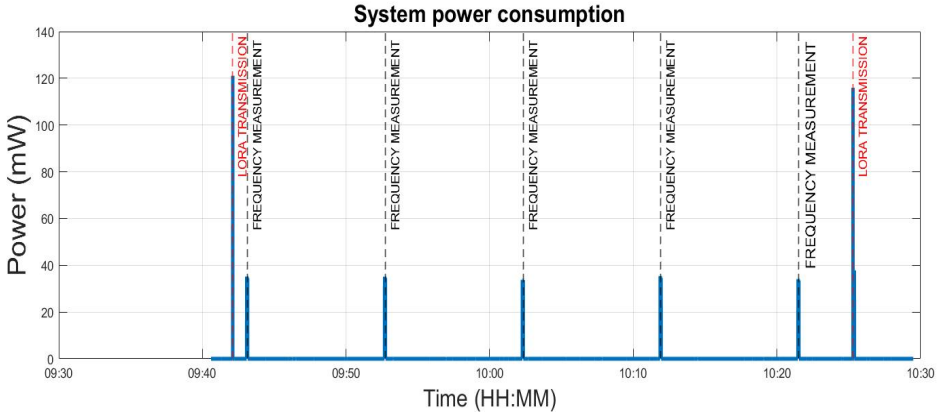

Figure 6.7: Power consumption sequence in a 51 min interval (15270 samples): the frequency measurement states are marked in black, while the LoRa transmission states are marked in red. The rest of the time the system is in stop mode. On the x-axis H = hours, M = minutes.

Table 6.1 resumes the average current and power requirements of the system in the different stages of the implemented power management strategy. The stop mode state duration is not reported since it corresponds to the intervals in between the other states and depends on the configuration set by the user. Given the duration (T in equation 6.2) of the data collection state and the LoRa transmission state, the energy consumption is evaluated as follow:

$$E = P \cdot T \tag{6.2}$$

Although the instantaneous current required by the LoRa transmission state is bigger than the frequency measurement state, this latter presents a higher energy consumption because of the longer time required to perform the operation, as reported in table 6.1

MCU state	Stop mode	Frequency measurement	LoRa transmission
Average current consumption	1.45 μA	10.5 mA	35 mA
Average power consumption	4.8 μW	34.5 mW	116 mW
Duration		3 s	$\sim$ 150 ms
Average energy consumption		103.5 mJ	17.4 mJ

Table 6.1: System consumption in the different power management strategy's states

6.2 PMFC-based energy harvester performance

After having analyzed the system power requirements, the PMFC-based energy harvester's capability of sustaining the receiving system's operation will be discussed in this section.

The 1 F supercapacitor attached to the VSTOR pin of the PMS is charged with the energy extracted from the PMFC in less than two days (about 42 hours), as can be observed in figure 6.8. The graph has been plotted by measuring the voltage on the VSTOR pin through a 34401A digital multimeter (Agilent Technologies) controlled with a LabVIEW script which is configured to sample the voltage value every 2 min. During the measurement, no circuit is attached to the VOUT pin of the PMS.

The startup operation explained BQ25570 datasheet ([38]) can be clearly observed in the VSTOR trend. Two are the circuit present in the PMS for boosting the input voltage: a low-power cold-start circuit and the high-efficiency main boost converter. When the voltage on VSTOR is lower than VSTOR_CHGEN (VSTOR $\leq$ VSTOR_CHGEN), the first option to charge the storage element attached to VSTOR is to start the cold-start circuit. If the energy harvester provides sufficient power to exit the cold start operation, when the supercapacitor voltage reaches VSTOR_CHGEN, the main boost regulator is turned on. As can be clearly observed in figure 6.8, the threshold value is VSTOR_CHGEN = 1.73 V. The supercapacitor charge is much slower until the voltage reaches VSTOR_CHGEN since it is done by the cold-start circuit, which is an unregulated boost converter with a lower efficiency with respect to the main boost converter. When the threshold value is reached, the main boost converter starts up, and the

voltage on VSTOR starts to increase much faster.
When the storage element is attached to the PMS, it is almost completely discharged ($V_{store} = 0.054$ V). The energy extracted from the PMFC charges it up to $V_{store} = 4.18$ V, as configured by the producer of the BQ25570 evaluation module.

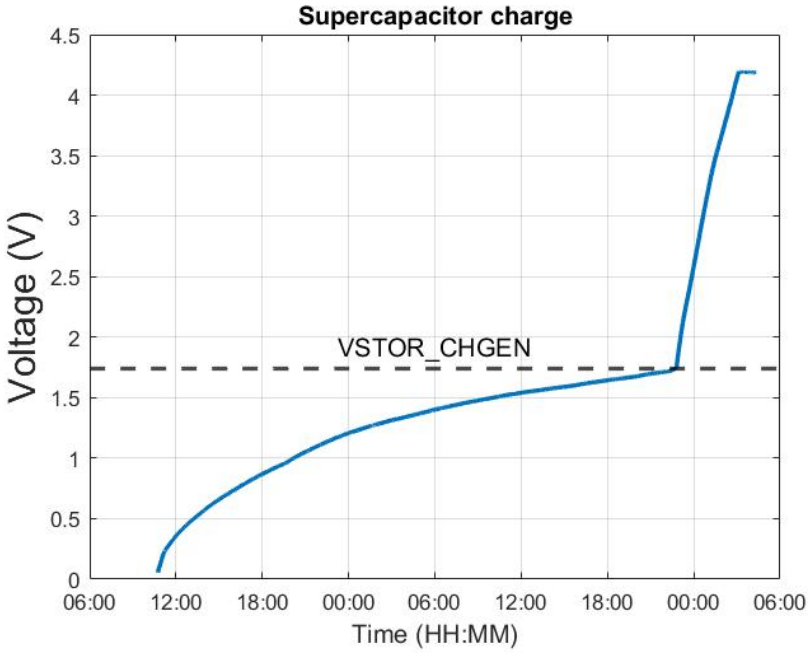

Figure 6.8: Charge of the supercapacitor through the PMFC-based energy harvesting system. On the x-axis H = hours, M = minutes.

6.2.1 System autonomy

In order to demonstrate the receiving system autonomy, the voltage on the supercapacitor (V_{store}) has been monitored during about 19 hours of system operation. Data are again acquired with a 34401A multimeter from Agilent Technologies controlled with a LabVIEW script, sampling the voltage value every 1 s.
The complete system has been mounted as shown in figure 6.1. The transmitting system has been configured to generate a square wave between 0 V and 3.3 V, with a frequency proportional to the plant stem impedance (as explained in section 4.9). The period between the generation of a signal and the following is 30 min, so the receiving system is awakened every $T_{meas} = 30$ min to perform a frequency measurement. The transmission duty cycle is set to $T_{TX} = 1$ hour, so a LoRa packet is sent to the gateway with this periodicity.

Figure 6.9 shows the voltage trend on the supercapacitor during the 19 hours of monitoring. As can be observed, when the measurements start, the supercap. is not completely charged, indeed the voltage on VSTOR is $V_{store} \simeq 3.95$ V. From the general trend, it can be observed that the energy harvested from the PMFC amply satisfies the sensor node's potential requirements for measuring and communicating. Indeed, with the configured periodicity of data collection and transmission, the PMFC provides enough energy to charge the supercap. up to $V_{store} = 4.2$ V, and, once reached, to remain around this value of voltage. When the microcontroller unit that is attached to the VOUT pin of PMS wakes up, the current is drawn from the supercap. which discharges partially. These voltage drops will be better shown in the following figures.

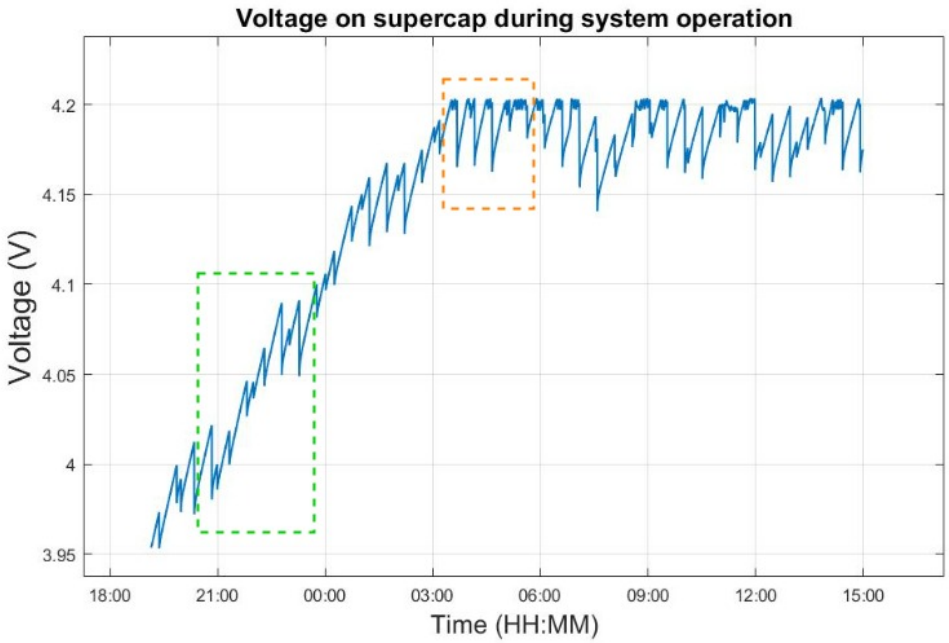

Figure 6.9: Voltage on the storage element attached to the PMS while sustaining the receiving system operation. The monitoring interval is about 19 hours (70878 samples). The green rectangle part is zoomed in figure 6.10, while the orange rectangle part in figure 6.13. On the x-axis H = hours, M = minutes.

Figure 6.10 shows a zoomed view of the voltage in the green rectangle in figure 6.9. The voltage drops due to the awakening of the MCU to perform the frequency measurement are marked with vertical black lines. It can be observed this event is repeated every $T_{meas} = 30$ min. As already stated in 6.1, even if the most power-consuming state is the transmission of the LoRa payload, it can be clearly

deduced from the figure that the frequency measurement state is the one that causes the highest voltage drop on the supercap. because of its longest duration. When the system returns in stop mode, the PMS has a loading circuit on the VOUT pin which consumes only $P_{stop} \simeq 4.8\ \mu W$ of power, thus it is able to charge the supercap. with a slope $\frac{\Delta V}{\Delta t} \simeq 0.35$ mV/s.

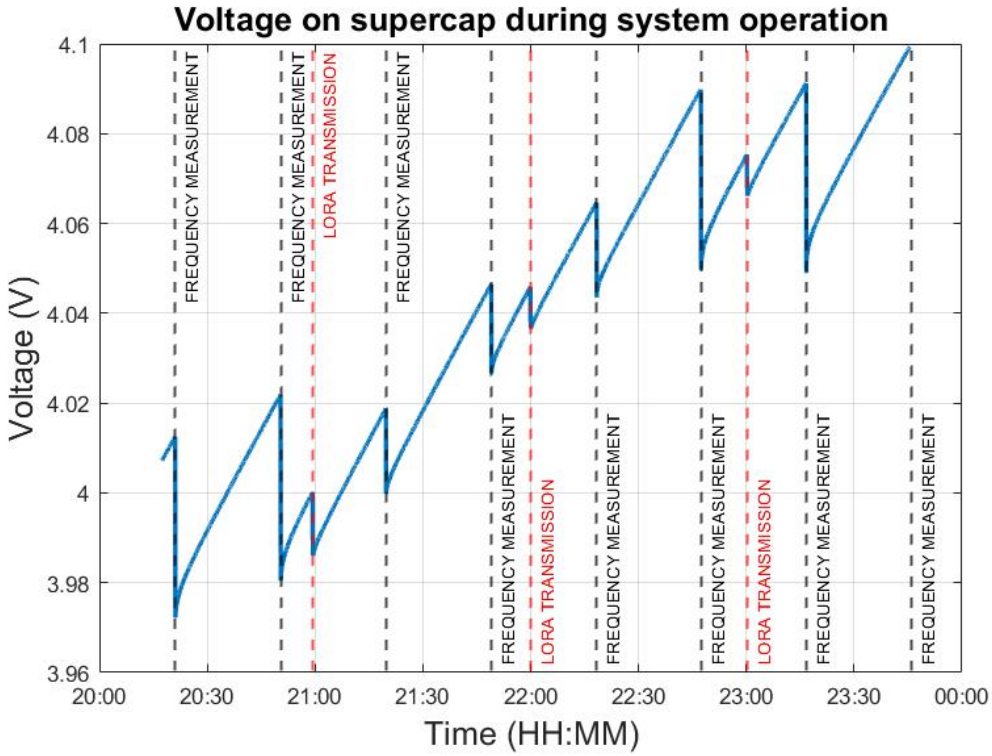

Figure 6.10: Voltage on the storage element attached to the PMS while sustaining the receiving system operation. The monitoring interval is 206 minutes (12360 samples). On the x-axis H = hours, M = minutes.

One example of voltage drop on the supercap. due to the awakening of the system by the oscillating signal is shown in figure 6.11. In figure 6.11 the voltage drop on VSTOR is $\Delta V \simeq 40$ mV. Considering all the voltage drops acquired during the monitoring due to the frequency measurement, the average voltage drop is $\Delta V \simeq 30$ mV. This is in accord with the current values reported in table 6.1. Indeed, with the hypothesis of supercap. discharge at constant current, the voltage drop can be evaluated as follow:

$$\Delta V = \frac{\Delta Q}{C} \tag{6.3}$$

where C is the supercap. capacitance, C = 1 F. The lost charge ΔQ can be

approximately evaluated as:

$$\Delta Q = I \cdot \Delta t \tag{6.4}$$

where I is the constant current and Δt the duration of the voltage drop. From relations 6.3 and 6.4, the voltage drop is:

$$\Delta V = \frac{I \cdot \Delta t}{C} \tag{6.5}$$

Considering the frequency measurement state, given I $\simeq$ 10.5 mA, Δt $\simeq$ 3 s and C = 1 F, the voltage drop value obtained with relation 6.5 is ΔV $\simeq$ 30.5 mV. This value corresponds to the average voltage drop extracted from the graph. However, since the periodicity with which samples are acquired (1 s) is large with respect to the state duration, not all the voltage drops correspond exactly to this value, but they can be smaller (20 mV) or bigger (40 mV).

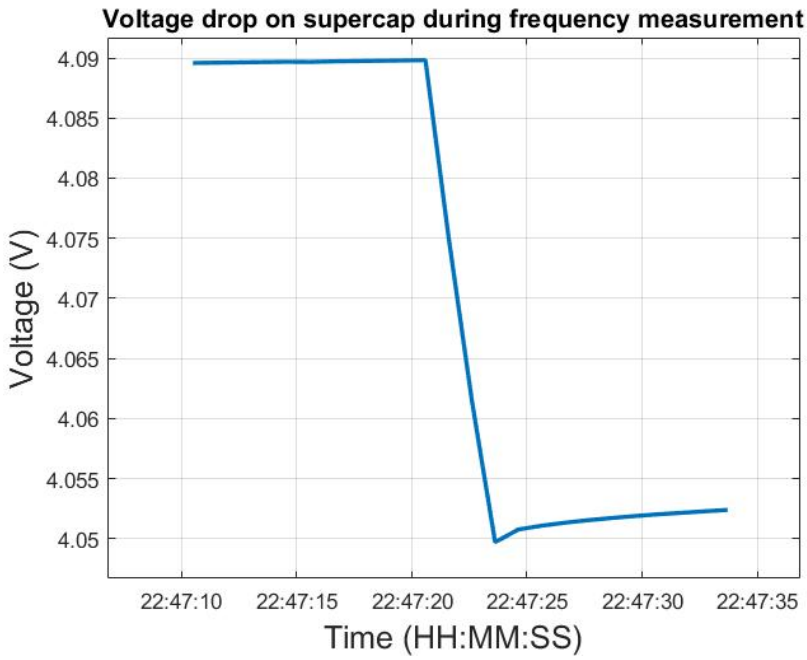

Figure 6.11: Voltage drop on the supercapacitor due to the awekening of the microcontroller unit attached to VOUT pin to perform a frequency measurement. On the x-axis H = hours, M = minutes, S = seconds.

In figure 6.12 the voltage drop on the VSTOR caused by a LoRa packet transmission is shown. As clearly visible in figure 6.6, also in this figure, it is possible to observe the first voltage drop due to the data transmission to the gateway and a

smaller subsequent drop caused by the two downlink receive windows. From both figures can be deduced that the receive windows are opened about 5 s after the transmission window. In this interval, the supercap. restarts to charge, before discharging again.
The average voltage drop among all the observed LoRa transmissions is $\Delta V \simeq 7$ mV. Given I $\simeq$ 35 mA, $\Delta t \simeq 150$ ms and C = 1 F, from the relation 6.5 it is possible to evaluate that the voltage drop for a LoRa transmission is $\Delta V \simeq 5.25$ mV. This value corresponds approximately to the average voltage drop value deduced from the plot (7 mV). In this case, the voltage values reported in the graph are even less precise than the evaluation carried out for the frequency measurement state since the duration of the LoRa transmission is much smaller than the sampling period.

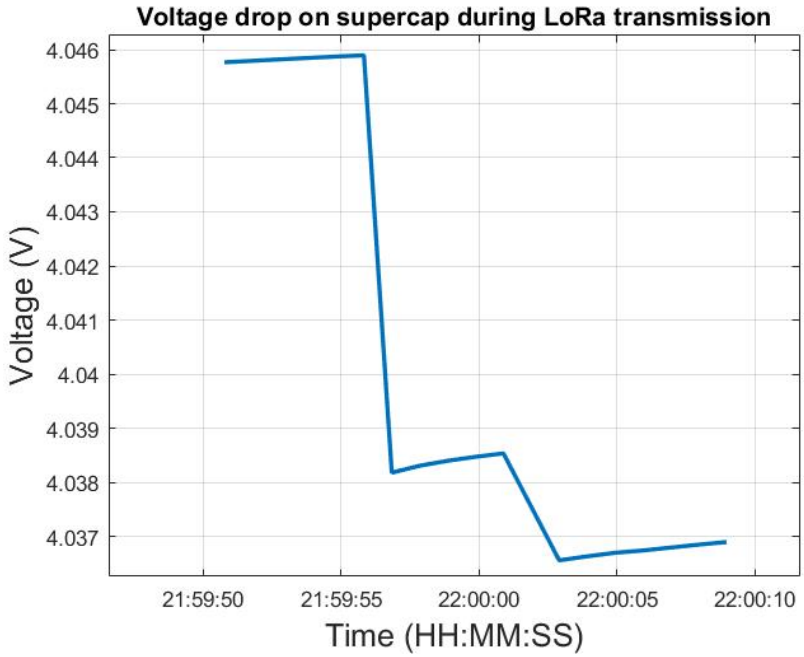

Figure 6.12: Voltage drop on the supercapacitor due to the awekening of the microcontroller unit attached to VOUT pin to perform Lora transmission. On the x-axis H = hours, M = minutes, S = seconds.

Figure 6.13 shows a zoomed view of the voltage trend part in the orange rectangle in figure 6.9. As can be observed, when these samples are acquired, the supercap. voltage is around the maximum deliverable value on VSTOR, that is $V_{store} \simeq 4.2$ V. In addition to the previously mentioned voltage drops, many other drops can be noticed around 4.2 V. This behavior of the voltage on VSTOR can be explained with the protection of the storage element from overcharging performed by the

BQ25570 power management system. Indeed, as can be read in [38], when the voltage on VSTOR reaches the OV condition, the main boost converter is disabled. Thus, as better shown in figure 6.14, the voltage on the supercap. increases up to $V_{store} \simeq 4.203$ V, when the boost converter is deactivated. Then it starts decreasing for about 1 min (even if each of these drops has a variable duration) down to $V_{store} \simeq 4.197$ V, and, when reached this value, starts to increase again.

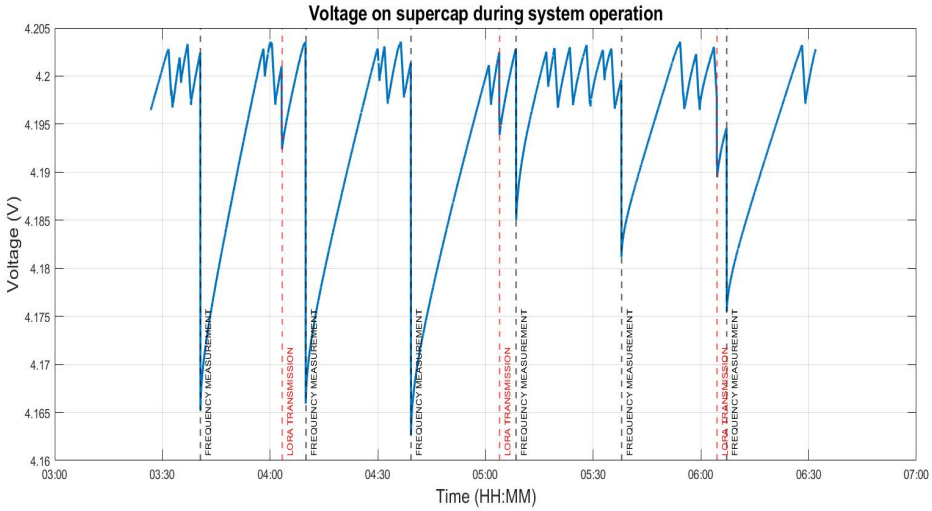

Figure 6.13: Voltage on the storage element attached to the PMS while sustaining the receiving system operation. The monitoring interval is 183 minutes (11000 samples). On the x-axis H = hours, M = minutes.

The operation of the complete sensor node has been sustained since its setup for 12 days by the two energy harvesting systems (PMFC and solar cells). Especially for the energy extracted from the PMFC, it can be observed that it enables an autonomous operation of the receiving system with extremely good efficiency. Indeed, with the configured timing parameters, data are collected every 30 minutes and sent to the gateway to be analyzed every 1 hour. However, given the slow variation of the measured parameter (plant stem electrical impedance) during a day, the periodicity of these events could also be enlarged, enhancing the lifetime of the sensor node.

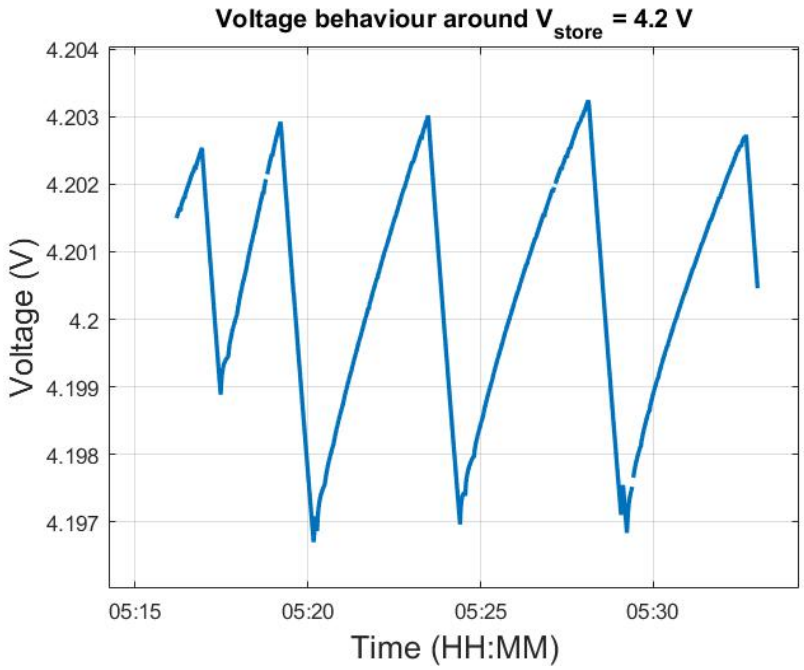

Figure 6.14: Voltage drops registered around V_{store} V due to the overcharge protection mechanism of the PMS. On the x-axis H = hours, M = minutes.

6.3 Live data analysis

In order to analyze the LoRa packets sent to the gateway, they can be collected using The Things Network (TTN) console. This network server provides the possibility to build an IoT application at a low cost and with maximum security thanks to end-to-end encryption. TTN aims to build a collaborative, global LoRaWAN network. The end nodes send packets that are received by the local gateway and forwarded by this latter to TTN through Ethernet/WiFi/3G/4G connection. The row payload received by TTN is decoded with a simple Javascript code so that data are shown in the TTN console in an easily readable way.

The first data collection has been performed using a B-L072Z-LRWAN1 Discovery kit from STMicroelectronics instead of the custom board since this latter was not ready yet. It embeds the CMWX1ZZABZ-091 LoRa module from Murata (as the custom board) and the STM32L072CZY6 microcontroller (the same series of the microcontroller embedded in the custom board). The board was powered through a bench power supply since the cell was not performing well in that period. The transmitting power was powered by the solar cells.
The application was configured to send a LoRa packet every 1 hour, while frequency

measurements were performed every 30 minutes so that the payload is constituted by the average of two frequency values. Data were collected for about four days, and the obtained results are shown in figure 6.15. The moving mean in a window of 7 elements was plotted to reduce the spikes.
The frequency values vary between 12 kHz and 34 kHz. The signal coming from the plant has, as can be clearly observed in the figure, the same daily pattern in all four days of monitoring. It is connected with the drying process that the plant undergoes as a consequence of the variation of temperature during the day. In particular, the signal's frequency tends to increase when the temperature decreases and decrease towards the hottest hours of the day (around 12:00). This is consistent with the results obtained in the analysis carried out in [35]. Indeed the authors observed a steady increase in the impedance modulus following the plant drying process. An impedance increase corresponds to a decrease in the frequency being inversely proportional to the stem impedance through relation 4.1.

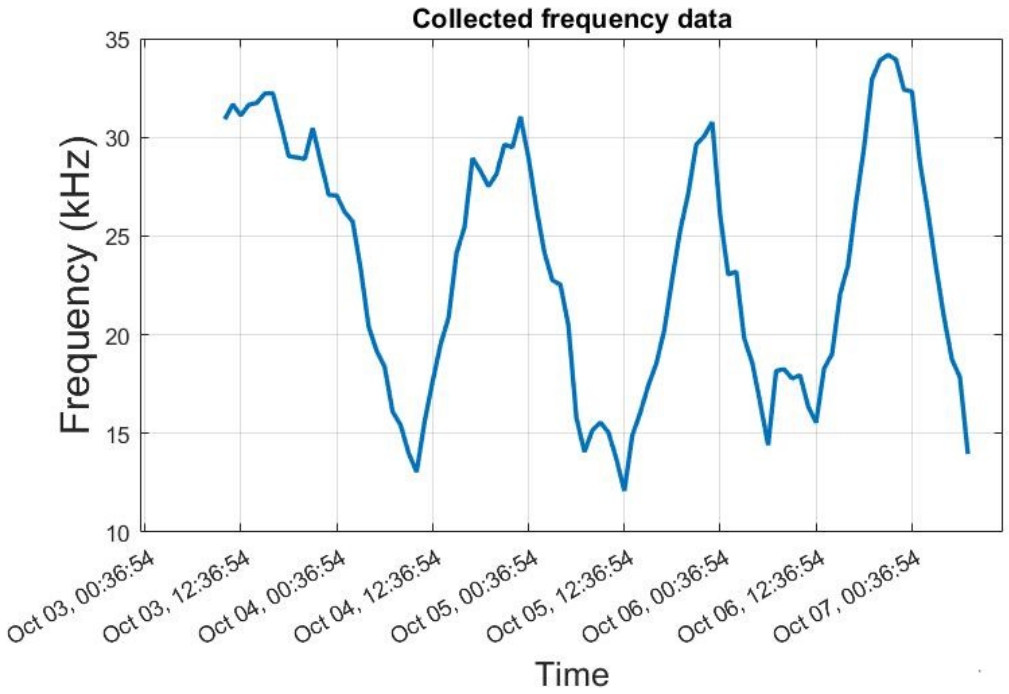

Figure 6.15: Frequency data collect during 4 days of plant monitoring.

During the sensor node operation presented in 6.2.1, frequency data have been collected a second time. The obtained values in a period of 12 days are plotted in figure 6.16. In order to remove the few spikes registered in the frequency values

(probably due to some code's bugs), the moving average has been plotted considering a window of 5 elements.
During the monitoring period, the plant was never water. Thus an overall decrease of the frequency values due to the plant drying process was expected to be observed. Nevertheless, as can be noticed, the collected data show an increasing trend. Moreover, the periodic daily pattern observed in figure 6.15 is not visible in this plot. This leads to the conclusion that the collected data are not sufficient to understand the plant health status. The sensor node must be improved to have useful information that allows to make decisions about watering planning and prevent possible plant diseases. The possible improvements will be explained in section 6.4.
With respect to the previously collected data (figure 6.15), the range of measured frequency is shifted towards higher values. Indeed, as can be observed in figure 6.16, the minimum frequency is around 44 kHz, while the maximum is around 62 kHz. This shift has been achieved by reducing the value of the capacitance C in relation 4.1, so to increase the generated signals' frequency. This has been done to avoid working around frequency values close to the cut-off frequency (10 kHz) of the high-pass filter introduced in 4.2.3.

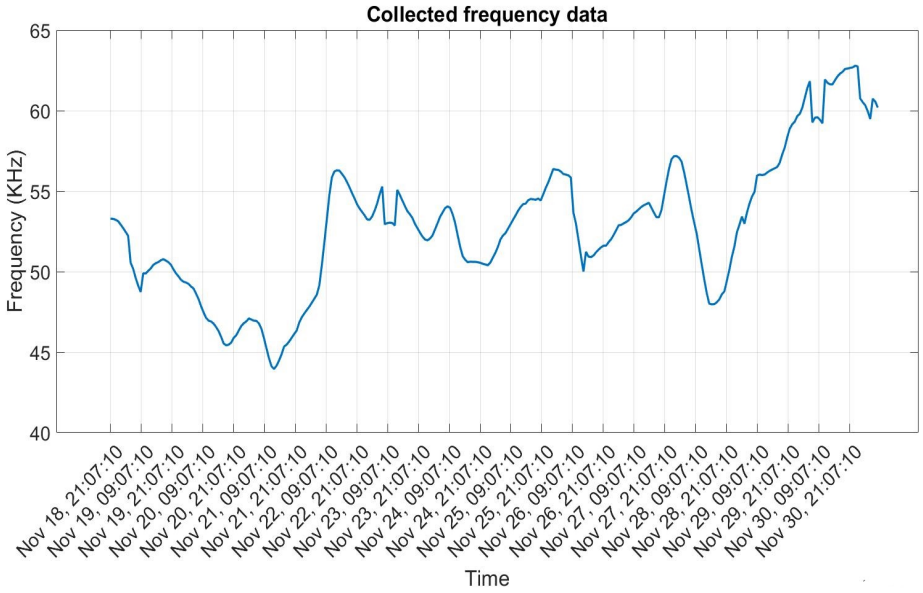

Figure 6.16: Frequency data collected in 12 days of complete system operation.

6.4 Future improvements

Some measures can be taken in the future in order to enhance further the efficiency and the durability of the implemented system. In this section, the possible improvements and the reasons behind them will be presented.

6.4.1 PMFC's electrodes

The choice of the cell electrodes is of fundamental importance for maximizing the power extraction and the durability of the harvesting system. The use of Cu-Zn electrodes has been demonstrated to produce highly satisfying levels of energy. Nevertheless, as stated in Chapter 3, the durability of the cell is significantly compromised by the degradation of the electrodes in a relatively small period. Thus the implemented PMFC can be improved by choosing electrodes' materials that do not undergo oxidation or that can ensure a correct operation for a longer time. Even better would be to use biodegradable and eco-friendly materials.

6.4.2 Plant health monitoring

In order to have a complete understanding of the plant health status, the monitoring of the plant impedance changes alone is not sufficient. Indeed, as already stated in 4.1, the direct inspection method employed by the present sensor node is capable of giving a punctual knowledge of what happens inside the plant stem, but this is not straightforward. In order to obtain useful information, the relation between the impedance changes and the hydration status must be understood. Thus, the improvement that could be made to the system is the addition of a soil moisture sensor. The combined analysis of these two parameters would be useful to analyze the irrigation effect on the plant's electrical characteristics.

Chapter 7

Conclusions

A completely self-autonomous sensor node for plant health monitoring was proposed in this dissertation. The bioelectricity production has been achieved with an emergent green technology, known as Plant Microbial Fuel Cell, which takes advantage of the microbial activity at the plant's rhizosphere region. The cell has been constructed by placing Cu-Zn electrodes in the soil inside a plastic pot with tobacco plants.
The choice of ultra-low-power hardware components has enabled a power consumption of only 4.8 μW when the system is in the idle state, which ensures an extended node lifetime. Thanks to the adoption of a power management strategy, the experimental results have demonstrated the balancing of the system potential requirements with the energy levels extracted from the PMFC.
Live data from the sensor node have been collected and analyzed to extract information about the health status of a tobacco plant. However, further studies, supported by the combined analysis of the plant stem impedance and soil moisture, are needed to understand the relationship between the plant's electrical characteristics and its health status.

Bibliography

[1] «Selected Results of the 2019 UN World Population Projections». In: *Population and development review* 45 (2019), pp. 689–694 (cit. on p. 1).

[2] Nabil Swedan. «Deforestation and land farming as regulators of population size and climate». In: *Acta ecologica Sinica* 40 (2020), pp. 443–450 (cit. on p. 1).

[3] Ultan Mc Carthy, Ismail Uysal, Ricardo Badia-Melis, Samuel Mercier, Colm O'Donnell, and Anastasia Ktenioudaki. «Global food security – Issues, challenges and technological solutions». In: *Trends in food science and technology* 77 (2018), pp. 11–20 (cit. on p. 2).

[4] J Rockstrom, J Williams, G Daily, A Noble, N Matthews, L Gordon, H Wetterstrand, F DeClerck, and C.M.S Fraiture de. «Sustainable intensification of agriculture for human prosperity and global sustainability». In: *Ambio* 46 (2017), pp. 4–17 (cit. on pp. 2, 3).

[5] L.F Bergstrom. «Food production for a growing world population: The impact of food production on soils and groundwater resources». In: *Journal of food science* 69 (2004), R181–R184 (cit. on p. 2).

[6] Food and Agriculture Organization (Fao). «Coping with Water Scarcity: An Action Framework for Agriculture and Food Security: Fao Water Reports No 38». In: (2013) (cit. on p. 2).

[7] Pisana Placidi, Renato Morbidelli, Diego Fortunati, Nicola Papini, Francesco Gobbi, and Andrea Scorzoni. «Monitoring soil and ambient parameters in the iot precision agriculture scenario: An original modeling approach dedicated to low-cost soil water content sensors». In: *Sensors (Basel, Switzerland)* 21 (2021), p. 5110 (cit. on p. 3).

[8] Mohamed Idbella, Mariano Iadaresta, Graziano Gagliarde, Alberto Mennella, Stefano Mazzoleni, and Giuliano Bonanomi. «Agrilogger: A new wireless sensor for monitoring agrometeorological data in areas lacking communication networks». In: *Sensors (Basel, Switzerland)* 20 (2020), p. 1589 (cit. on pp. 4, 7).

[9] Jorge Martínez-Guanter, Miguel Garrido-Izard, Constantino Valero, David C Slaughter, and Manuel Pérez-Ruiz. «Optical sensing to determine tomato plant spacing for precise agrochemical application: Two scenarios». In: *Sensors (Basel, Switzerland)* 17 (2017), p. 1096 (cit. on pp. 4, 6).

[10] Abdelaziz M Okasha, Hasnaa G Ibrahim, Adel H Elmetwalli, Khaled Mohamed Khedher, Zaher Mundher Yaseen, and Salah Elsayed. «Designing low-cost capacitive-based soil moisture sensor and smart monitoring unit operated by solar cells for greenhouse irrigation management». In: *Sensors (Basel, Switzerland)* 21 (2021), p. 5387 (cit. on p. 4).

[11] Tomáš Syrový, Robert Vik, Silvan Pretl, Lucie Syrová, Jiří Čengery, Aleš Hamáček, Lubomír Kubáč, and Ladislav Menšík. «Fully printed disposable IoT soil moisture sensors for precision agriculture». In: *Chemosensors* 8 (2020), pp. 1–14 (cit. on pp. 4, 5).

[12] Jirapond Muangprathub, Nathaphon Boonnam, Siriwan Kajornkasirat, Narongsak Lekbangpong, Apirat Wanichsombat, and Pichetwut Nillaor. «IoT and agriculture data analysis for smart farm». In: *Computers and electronics in agriculture* 156 (2019), pp. 467–474 (cit. on p. 5).

[13] S Askraba, A Paap, K Alameh, J Rowe, and C Miller. «Laser-Stabilized Real-Time Plant Discrimination Sensor for Precision Agriculture». In: *IEEE sensors journal* 16 (2016), pp. 6680–6686 (cit. on p. 6).

[14] S Sudevalayam and P Kulkarni. «Energy Harvesting Sensor Nodes: Survey and Implications». In: *IEEE Communications surveys and tutorials* 13 (2011), pp. 443–461 (cit. on p. 9).

[15] C Alippi, R Camplani, C Galperti, and M Roveri. «A Robust, Adaptive, Solar-Powered WSN Framework for Aquatic Environmental Monitoring». In: *IEEE sensors journal* 11 (2011), pp. 45–55 (cit. on p. 10).

[16] Yin Li and Ronghua Shi. «An intelligent solar energy-harvesting system for wireless sensor networks». In: *EURASIP journal on wireless communications and networking* 2015 (2015), pp. 1–12 (cit. on p. 10).

[17] S Chamanian, S Baghaee, H Ulusan, O Zorlu, E Uysal-Biyikoglu, and H Kulah. «Implementation of Energy-Neutral Operation on Vibration Energy Harvesting WSN». In: *IEEE sensors journal* 19 (2019), pp. 3092–3099 (cit. on p. 10).

[18] Yen Kheng Tan and Sanjib Kumar Panda. «Optimized Wind Energy Harvesting System Using Resistance Emulator and Active Rectifier for Wireless Sensor Nodes». In: *IEEE transactions on power electronics* 26 (2011), pp. 38–50 (cit. on p. 11).

[19] David P. B. T. B Strik, H. V. M Hamelers (Bert), Jan F. H Snel, and Cees J. N Buisman. «Green electricity production with living plants and bacteria in a fuel cell». In: *International journal of energy research* 32 (2008), pp. 870–876 (cit. on pp. 11, 16, 17).

[20] M. C. Potter. «Electrical effects accompanying the decomposition of organic compounds». In: *Proceedings of the Royal Society B: Biological Sciences* 84 (1911), pp. 260–276 (cit. on p. 11).

[21] Zhuwei Du, Haoran Li, and Tingyue Gu. «A state of the art review on microbial fuel cells: A promising technology for wastewater treatment and bioenergy». In: *Biotechnology advances* 25 (2007), pp. 464–482 (cit. on pp. 12–14).

[22] Bruce E Logan, Bert Hamelers, René Rozendal, Uwe Schröder, Jürg Keller, Stefano Freguia, Peter Aelterman, Willy Verstraete, and Korneel Rabaey. «Microbial Fuel Cells: Methodology and Technology». In: *Environmental science and technology* 40 (2006), pp. 5181–5192 (cit. on p. 12).

[23] M.M Ghangrekar and V.B Shinde. «Performance of membrane-less microbial fuel cell treating wastewater and effect of electrode distance and area on electricity production». In: *Bioresource technology* 98 (2007), pp. 2879–2885 (cit. on p. 12).

[24] Bruce E Logan and John M Regan. «Electricity-producing bacterial communities in microbial fuel cells». In: *Trends in microbiology (Regular ed.)* 14 (2006), pp. 512–518 (cit. on p. 14).

[25] Rachnarin Nitisoravut and Roshan Regmi. «Plant microbial fuel cells: A promising biosystems engineering». In: *Renewable and sustainable energy reviews* 76 (2017), pp. 81–89 (cit. on pp. 15, 22).

[26] Ke Zhang, Xiangling Wu, Jia Chen, Wei Wang, Hongbing Luo, Wei Chen, Dandan Ma, Xiaochan An, and Zhaolan Wei. «The role and related microbial processes of Mn-dependent anaerobic methane oxidation in reducing methane emissions from constructed wetland-microbial fuel cell». In: *Journal of environmental management* 294 (2021), pp. 112935–112935 (cit. on p. 15).

[27] Han Xu, Hai-Liang Song, Rajendra Prasad Singh, Yu-Li Yang, Jia-Ying Xu, and Xiao-Li Yang. «Simultaneous reduction of antibiotics leakage and methane emission from constructed wetland by integrating microbial fuel cell». In: *Bioresource technology* 320 (2021), p. 124285 (cit. on p. 15).

[28] Korneel Rabaey and Willy Verstraete. «Microbial fuel cells: novel biotechnology for energy generation». In: *Trends in biotechnology (Regular ed.)* 23 (2005), pp. 291–298 (cit. on p. 16).

[29] M Helder, D.P.B.T.B Strik, H.V.M Hamelers, and C.J.N Buisman. «The flat-plate plant-microbial fuel cell: the effect of a new design on internal resistances». In: *Biotechnology for biofuels* 5.1 (2012), pp. 70–70 (cit. on p. 17).

[30] Davide Brunelli, Pietro Tosato, and Maurizio Rossi. «Microbial fuel cell as a biosensor and a power source for flora health monitoring». In: *2016 IEEE SENSORS*. IEEE, 2016, pp. 1–3 (cit. on pp. 17, 20).

[31] Davide Brunelli, Pietro Tosato, and Maurizio Rossi. «Flora Health Wireless Monitoring with Plant-Microbial Fuel Cell». In: *Procedia engineering* 168 (2016), pp. 1646–1650 (cit. on p. 17).

[32] Edith Osorio De La Rosa, Javier Vázquez Castillo, Mario Carmona Campos, Gliserio Romeli Barbosa Pool, Guillermo Becerra Nuñez, Alejandro Castillo Atoche, and Jaime Ortegón Aguilar. «Plant microbial fuel cells-based energy harvester system for self-powered IoT applications». In: *Sensors (Basel, Switzerland)* 19 (2019), p. 1378 (cit. on pp. 19, 23, 24).

[33] Hassel Aurora Alcalá-Garrido, Víctor Barrera-Figueroa, Mario E Rivero-Ángeles, Yunia Verónica García-Tejeda, and Hosanna Ramírez Pérez. «Analysis and Design of a Wireless Sensor Network Based on the Residual Energy of the Nodes and the Harvested Energy from Mint Plants». In: *Journal of sensors* 2021 (2021), pp. 1–26 (cit. on pp. 21, 24).

[34] Edith Osorio-de-la-Rosa, Javier Vazquez-Castillo, Alejandro Castillo-Atoche, Julio Heredia-Lozano, Andrea Castillo-Atoche, Guillermo Becerra-Nunez, and Romeli Barbosa. «Arrays of Plant Microbial Fuel Cells for Implementing Self-Sustainable Wireless Sensor Networks». In: *IEEE sensors journal* 21 (2021), pp. 1965–1974 (cit. on pp. 23, 24).

[35] Umberto Garlando, Lee Bar-On, Paolo Motto Ros, Alessandro Sanginario, Sebastian Peradotto, Yosi Shacham-Diamand, Adi Avni, Maurizio Martina, and Danilo Demarchi. «Towards Optimal Green Plant Irrigation: Watering and Body Electrical Impedance». In: *2020 IEEE International Symposium on Circuits and Systems (ISCAS)*. 2020, pp. 1–5 (cit. on pp. 32, 77).

[36] Paolo Motto Ros, Enrico Macrelli, Alessandro Sanginario, Yosi Shacham-Diamand, and Danilo Demarchi. «Electronic System for Signal Transmission Inside Green Plant Body». In: *2019 IEEE International Symposium on Circuits and Systems (ISCAS)*. IEEE, 2019, pp. 1–5 (cit. on p. 32).

[37] Stefano Calvo. *An energy autonomous electronic transmitting system for green plant sensing applications*. 2020 (cit. on pp. 32, 40, 41, 43, 45).

[38] *BQ25570 data sheet*. Texas Instruments, 2013 (cit. on pp. 34, 69, 75).

[39] *TPL5110 Nano-Power System Timer for Power Gating data sheet*. Texas Instruments, 2015 (cit. on p. 43).

[40] *LMC555 CMOS Timer data sheet*. Texas Instruments, 2020 (cit. on p. 43).

[41] *STM32 LoRaWAN® Expansion Package for STM32Cube User Manual*. STMicroelectronics, 2021 (cit. on pp. 47, 49).